EXPERIMENTAL INVESTIGATION ON THE EFFECT OF PORE STRUCTURE ON CAPILLARY TRAPPING IN 3D PRINTED POROUS MEDIA

A Thesis

by

ABDULLAH SHAAT

Submitted to the Graduate and Professional School of
Texas A&M University
in partial fulfillment of the requirements for the degree of

MASTER OF SCIENCE

Chair of Committee,	Nimir Elbashir
Co-Chair of Committee,	Nayef Alyafei
Committee Members,	Albertus Retnanto
Head of Department	Arul Jayaraman

December 2021

Major Subject: Chemical Engineering

ABSTRACT

As the global population increases with science and technology advancements, the energy demand continues to grow, which presents a generational challenge between energy production and climate change. Understanding capillary trapping in porous media and its implications would aid in meeting the increasing energy demands through enhanced oil recovery and reducing the carbon dioxide concentration in the atmosphere through CO_2 sequestration. Capillary trapping is a phenomenon caused by the displacement of the non-wetting phase by the wetting phase in the reservoir. Capillary trapping dictates the efficiency of enhanced oil recovery (EOR) and CCS.

The objective of this work was to study the relationship between the pore structure – in terms of the average coordination number and the average aspect ratio – and capillary trapping.

It was found that the average aspect ratio and average coordination number of a system directly influence capillary trapping. The higher the average aspect ratio, the higher the capillary trapping due to the difference in size between the pore and the surrounding throats. When the pore is significantly bigger in size than the throats, the non-wetting phase gets trapped in the pore due to the snap-off effect. On the contrary, capillary trapping decreases with the increase in coordination number value due to more throats connected to each pore, making mobility easier. The aspect ratio has more effect on the capillary trapping when compared to the coordination number. Additionally, this study shows that the higher the pore structure parameter, the higher the capillary trapping at higher initial gas (non-wetting phase) saturations. Based on the results of this work, the pore structure

parameter is recommended to be extracted using an extraction model that utilizes the maximal axis ball algorithm when compared to the medial axis algorithm. Moreover, an empirical equation, including the effect of pore structure, was formulated to estimate the trapping capacity of any water-wet system. The formulated equation was tested using one extraction method and showed significant agreement to two widely used capillary trapping estimation models.

DEDICATION

This thesis is dedicated to my parents, siblings, and friends who were with me every step of the way.

ACKNOWLEDGEMENTS

I want to thank my Supervisor and Co-Chair, Dr. Nayef Alyafei, for his guidance and support from my undergraduate studies until the last day of my graduate studies. My committee Co-Chair, Dr. Nimir Elbashir, and committee member Dr. Albertus Retnanto for their constructive feedback and guidance through my graduate studies.

I also want to thank those who helped me academically and professionally, such as Dr. Thomas Seers, Mr. Talha Khan, Mr. Ibrahim Maghrabi, and Dr. Harris Rabbani.

I am also grateful to all the Chemical Engineering faculty and staff.

Lastly, I would like to thank Qatar National Research Fund for sponsoring my studies and funding the project, and Texas A&M University at Qatar for providing me with this opportunity.

CONTRIBUTORS AND FUNDING SOURCES

Contributors

This work was supported by a thesis committee, chaired by Professor Nimir Elbashir of the Department of Chemical Engineering, co-chaired by Associate Professor Nayef Alyafei of the Petroleum Engineering Department, and Professor Albertus Retnanto, the Program Chair of the Petroleum Engineering Department at Texas A&M University.

The 3D printing, machining, and execution of the experiment in Chapter 4 were assisted by Professor Thomas Seers, Ibrahim Almaghrabi, and Talha Khan of the Petroleum Engineering Department. Pore-network modeling in Chapter 4 was assisted by Visiting Lecturer, Harris Rabbani.

All other work conducted for the thesis (or) dissertation was completed by the student, Abdullah Shaat, independently.

Funding Sources

Graduate study was supported by Qatar National Research Fund, QNRF, project number NPRP12S-0227-190172.

NOMENCLATURE

Symbol	Description	SI Units
$\sigma_{SC.CO_2-B}$	The interfacial tension between supercritical carbon dioxide and brine	N/m
θ	The angle between the droplet and the solid surface	°
P_c	Capillary pressure	Pa
P_{nw}	Non-wetting phase pressure	Pa
P_w	Wetting phase pressure	Pa
σ	Interfacial tension	N/m
S_{nwr}	Non-wetting phase residual saturation	-
S_{nwi}	Non-wetting phase initial saturation	-
r_p	Pore radius	μm
r_t	Throat radius	μm
a	Aspect ratio	-
n_P	Total number of pores	-
C_N	Coordination number	-
n_t	Total number of throats connected to a specific pore	-
C_{trap}	Trapping capacity	-
ϕ	System effective porosity	-
S^*_{gr}	Effective residual gas saturation	-

Symbol	Description	SI Units
S^*_{gi}	Effective initial gas saturation	-
S_{wci}	Irreducible water saturation	-
C	Land's constant	-
$\propto$	Spiteri's first constant	-
β_s	Spiteri's second constant	-
J	Diffusion flux	mol/s
$D_{Knudsen}$	Knudsen diffusivity	m^2/s

TABLE OF CONTENTS

Page

LIST OF FIGURES

Page

LIST OF TABLES

Page

1. BACKGROUND

As the world advances in technology, science, economy, the global population continues to increase. Therefore, the energy demand will continue to grow. Energy demand is predicted to increase by 30% by the year 2040 (Jacobs, 2020). The oil and gas industry provides most of the global energy needs with over 50% of the worldwide energy consumption, while coal provides over 25% of total consumption, despite the efforts towards renewable energy resources (Jacobs, 2020).

However, with the increase in energy demand, there is an increase in climate change awareness, which is a significant generational challenge (Stocker & Xia, 2013). Fossil fuel energy systems produce greenhouse gases, including carbon dioxide, which is the most effective gas on climate change (Alley et al., 2007). Global mean temperature rise was directly correlated to increased carbon dioxide concentrations (Friedlingstein et al., 2010). Ideally, using renewable energy resources to meet the world energy demand would drastically reduce the carbon dioxide concentration. However, the world, especially developing countries, is still not prepared to abandon cheap fossil fuels and entirely depend on renewables (Tohidi et al., 2010).

Understanding multiphase fluid displacements in porous media and their implications would aid in meeting the increasing energy demands, enhanced oil recovery, and reduced carbon dioxide concentration in the atmosphere. After primary (first production stage) and secondary (second production stage) recoveries, trapped remains in the pores. The amount of trapped oil mainly depends on wettability, properties of the displacing and displaced fluids, and pore size

distribution (Hernandez et al. (2015), Mahani et al. (2015); Joekar-Niasar et al. (2008); Joekar Niasar (2010)). Altering the capillary trapping can significantly increase oil mobility and recovery (Morrow et al., 1986). Controlling the capillary trapping also improves the Carbon Capture and Storage (CCS) process, a carbon dioxide sequestration process (Gibbins & Chalmers, 2008). Carbon dioxide sequestration provides reservoir pressure support during the production period, which depends on the containment capacity and the injectivity (Schembre-McCabe et al., 2007).

Wettability is the preference of a solid surface to be in contact with one fluid over another present fluid. In an oil-water system, water-wet rocks prefer to be in contact with water over oil. Water imbibes the oil from the pores and the surface of the rock (Anderson, 1986a). Wettability depends on reservoir mineralogy, adsorption of hydrocarbon constituents, and the spreading capability of the oil phase (Agbalaka et al., 2008). Altering the wettability will impact capillary pressure and capillary trapping (Alnoush et al., 2021).

Capillary trapping is a phenomenon that traps the non-wetting phase and occurs due to the displacement of the non-wetting phase by the wetting phase in a porous medium. The non-wetting phase becomes trapped due to the capillary pressure, which reduces the non-wetting phase extraction capacity (Tanino & Blunt, 2013). Capillary trapping is an essential phenomenon that controls the effectiveness of storing oil or carbon dioxide in the reservoir by increasing the capillary trapping effects. Understanding capillary trapping also improves the quality of the enhanced

oil recovery (EOR) methods by reducing or controlling the capillary forces in the reservoir. Residual saturation is achieved through snap-off, piston-like, Haines jump, corner flow, or cooperative pore filling (Rabbani et al., 2017). Capillary trapping is affected by the capillary pressure, the fluid relative-permeability, and the contact angle, resulting from the reservoir wettability, as previously mentioned (Alyafei, 2019). To investigate the effect of pore structure on capillary trapping, an extensive review of wettability, capillary pressure, capillary trapping, and relative permeability curves must be conducted.

2. LITERATURE REVIEW

In porous geological media, two-phase fluid displacement is a mechanism with wide-ranging implications on energy and the environment. Water progresses across the pore space of hydrocarbon reservoirs as oil or gas is produced. Due to local capillary forces, this method of water imbibition can result in hydrocarbon trapping on the pore scale, a process known as capillary trapping (Tanino & Blunt, 2012). As a result, the subsurface could be stranded with valuable deposits of hydrocarbons. Capillary trapping can be visualized using the microcomputed tomography (Micro-CT) technology. Geological porous media can be used as a storage site for anthropogenic carbon dioxide (CO_2) emissions to limit the effect of these emissions on the environment (Alyafei, 2015). Capillary trapping dictates the ability of a reservoir to store the injected CO_2 and minimizing capillary trapping improves EOR.

2.1. Carbon Capture & Storage (CCS)

2.2. Carbon Dioxide Emissions and Climate Change

There is compelling evidence to show that human actions influence the earth's ecological mechanisms globally. The effect on the earth's carbon cycle of carbon dioxide (CO_2) pollution is an example (Alley et al., 2007; Falkowski et al., 2000).

The increased concentration of atmospheric CO_2 is associated with a mean rise in global temperature. A variety of variables impact the mean global temperature. Greenhouse gases are the most powerful, relying on the theory of radiative forcing, where CO_2 contributes the most due to its abundant presence (Alley et al., 2007). It

is projected that the effects of the resulting changes to the earth's climate environment will be significant unless the CO_2 content in the atmosphere is stabilized or even reduced (Alyafei, 2015). The attempts of reducing CO_2 pollution has been developed over the years. CCS depends on geological carbon dioxide sequestration, which is one of the main CO_2 pollution reduction processes (Hoffert et al., 2002; Wigley et al., 1996).

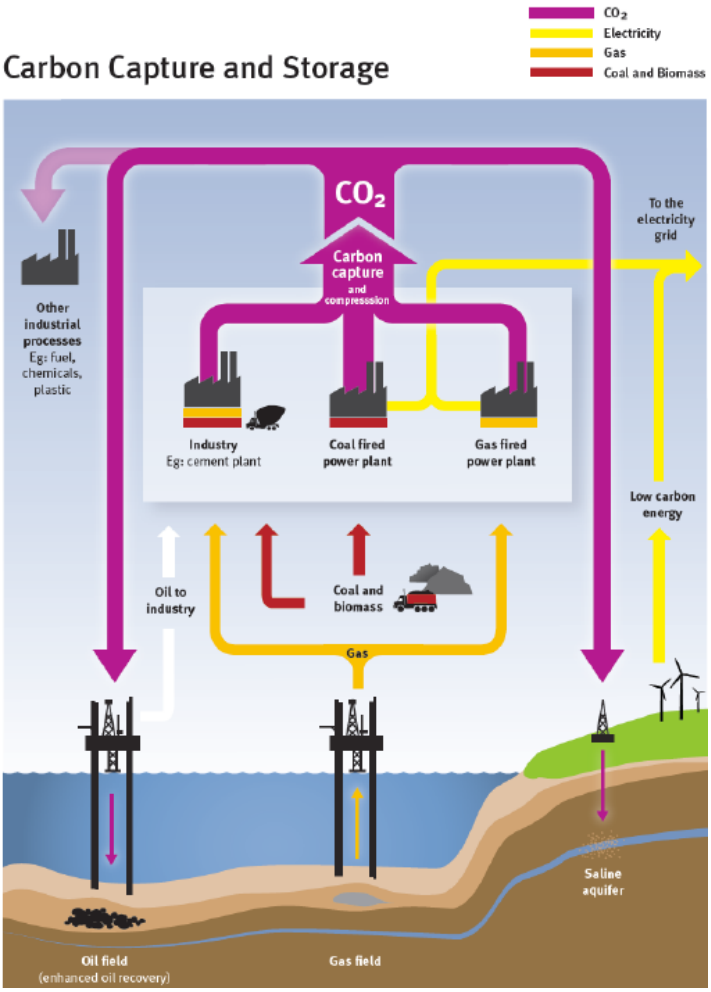

Figure 2.1: A schematic of CCS showing the collection of $\boldsymbol{CO_2}$ *and storing it or injecting it as part of enhanced oil recovery processes, obtained from Alyafei (2015).*

2.3. Subsurface Storage of CO_2 as a Prevention Method

Geological preservation of carbon dioxide refers to the mechanism in which geological formations, such as oil and gas reservoirs, saline aquifers, coal fields, and salt deposits (Lackner, 2003; OrrJr, 2004), CO_2 is retained for the long term. When CO_2 is injected into the reservoir with the aquifer, its mobility is governed by the solubility of CO_2 in brine, the phase viscosity and density, aquifer petrophysical properties, and the volume and injection rate of the CO_2 (Pentland et al., 2011). Hawkes et al. (2005) ranked sealine aquifers to be the top in terms of CO_2 storage capacity. CO_2 trapping mechanism can be classified into four groups: structural, dissolution, mineral, and capillary trapping.

2.3.1. Structural Trapping Mechanism

The hydrodynamic trapping mechanism occurs due to density-based differences. The caprock trapped the less-dense fluids, where the lighter fluids and the caprock pressure the denser fluids. Due to buoyancy forces, less dense CO_2 rises against the caprock. The success of this process depends upon the cap rock characterization (Bachu et al., 1994).

2.3.2. Dissolution Trapping Mechanism

Due to the solubility of CO_2 in water, CO_2 can be injected in the geological structure with brine, also known as solubility trapping, which is mainly affected by temperature and pressure. Solubility is measured through a tank designed to allow the suspended particles to settle at the bottom of the tank due to gravity. For instance, as described by Elbashir et al. (2002), a mixture of oil and solvent was

stirred for 15 at 275 rpm to ensure complete mixing with no oil loss. The mixture of oil and solvent was left to settle for 24 hours, leaving black sludge particles at the bottom of the tank. Then, the weight of the particles was recorded, and the oil and solvent mixture was removed from the sludge, which was later washed with n-hexane and 2-propanol to remove oil content in the sludge. Then the sludge was heated to remove excess solvents, which after the dry sludge was weighed. The percentage of lost oil was calculated by taking the difference between the weight of the wet sludge and the dry sludge and dividing it by the oil weight (Elbashir et al., 2002). The CO_2-soaked brine is denser than saturated brine (Lindeberg & Wessel-Berg, 1997). The denser CO_2-saturated brine migrates deeper into the structure and slowly dilutes. After injection of CO_2, this process begins, and its success depends upon the formation permeability, which is the ability of a rock to allow fluids to pass throw it (Ennis-King & Paterson, 2005).

2.3.3. Mineral Trapping Mechanism

Carbonic acid (H_2CO_3) is formed when CO_2 reacts with brine. Over long periods, typically hundreds of years, the formed species react with the host rock and brine. If the end-product of the reaction results in the formation of carbonate minerals, then it will result in a permanent CO_2 storage (Gunter et al., 1993).

2.3.4. Capillary Trapping Mechanism

The phenomenon of isolating the non-wetting phase through the wetting phase as trapped ganglia at the pore scale is known as capillary trapping (Tanino & Blunt, 2013). Miscible or immiscible displacement occurs when a porous medium's void

space is filled with two or more fluids. When the two fluids are entirely soluble in each other, and the interfacial stress between them is zero, miscible displacement occurs (Alyafei, 2019). A distinct phase interface appears in immiscible displacements, and there is no mass transfer through it. Immiscible displacements, under some circumstances, include oil-brine systems and supercritical CO_2-brine systems.

The capillary trapping mechanism is dependent on the displacement hysteresis and the capillary pressure characteristics of the CO_2-brine system. The capillary trapping mechanism involves trapping of CO_2 in the form of bubbles, which are immobile and surrounded by brine. It can occur over shorter timeframes than the other trapping mechanisms and is known to be significant (Rabbani et al., 2019).

Initially, in place, a large volume of the oil is not produced in oil fields because it has been trapped and made immobile because of the imbibing system of water flooding (Krevor et al., 2015). A phase diagram describing how the density and viscosity of CO_2 changes as a function of depth are shown below.

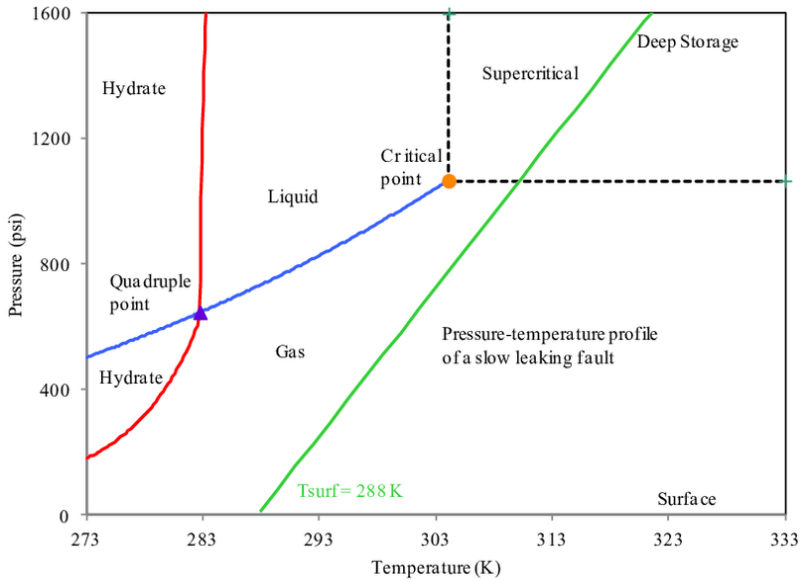

Figure 2.2: CO_2 *Phase diagram, obtained from Ramachandran et al. (2014).*

Supercritical CO_2 and brine are soluble, where the mass transfer occurs between the two phases after the injection of CO_2 into the reservoir aquifer. In the case of a CO_2-saturated brine, a region of the water aquifer, experiences immiscible displacement. The immiscible displacement occurs between the leading CO_2 plume edge and the wellbore region. Close to the wellbore, the injected CO_2 becomes undersaturated, and CO_2 dissolves into brine when it comes to contact with the undersaturated brine. Mass transfer in this zone depends on the reservoir geometry, porosity, permeability, rate of phase solubility, and the amount and rate of the injected CO_2 (Pentland et al., 2011). Mass transfer is governed by diffusivity and bulk flow (Clifford & Hillel, 1986). Therefore, the mass transfer is mainly through the Knudsen diffusion, where the system is at the scale of the free path of the particles. The Fick's law, the diffusivity parameter is then:

$$J = -D_{knudsen} \frac{dC_i}{dx} \quad (1)$$

Where J is the diffusion flux, $D_{Knudsen}$ is the diffusivity, which is affected by the pore size and temperature, C_i Is the concentration of a specific fluid, and x is the distance. For most CO_2 storage projects, the immiscible displacement area would be significantly greater in aquifer volume than the wellbore or leading-edge regions. The significant difference in the immiscible displacement area is due to the bubble entrapment dissolution and how it controls dissolved oxygen and the activity of anaerobic and aerobic microorganisms. It is, therefore, a crucial region for determining the capacity for CO_2 sequestration (R. Qi et al., 2009). In the immiscible displacement zone, the water phase is typically assumed as a continuous phase. The gas phase consists of trapped gas clusters, where the interphase mass transfer is limited by the slow water diffusion (Geistlinger et al., 2014). The multicomponent mass transfer processes control the gas bubble growth, dissolution, and mobilization in the immiscible displacement region (Ronen et al., 1989). The dissolution processes are controlled by the gas phase change, where the occurrence of trapped and stable gas bubbles indicates a vanishing steady-state mass transfer. This means that the mass transfer rate from the water to gas bubble compensates for the dissolution rate. Otherwise, the trapped gas bubbles will dissolve due to the capillary pressure that slowly increases the partial pressure inside the gas bubble (Geistlinger et al., 2005; Ronen et al., 1989). One of the key parameters that dictate the mass transfer rate is the interface between gas and water.

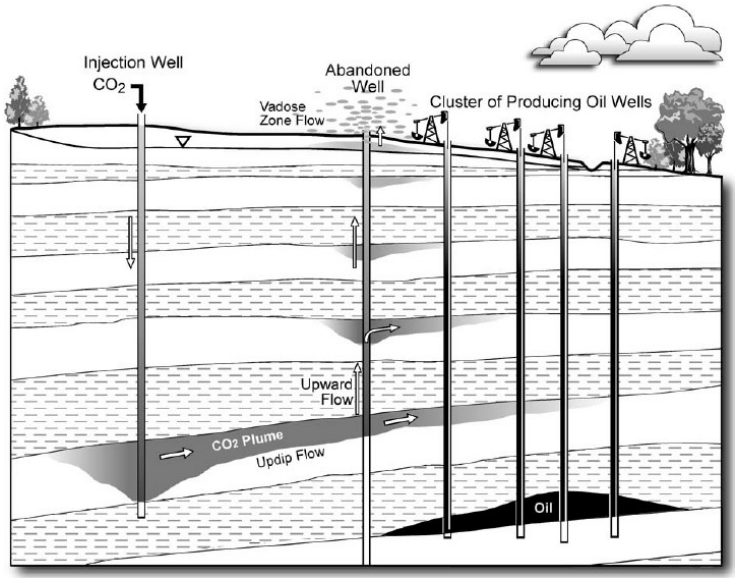

Figure 2.3: Formation water reacts with freshly injected (dry) CO_2 near the wellbore region. Equilibration of CO_2 and brine occurs, and the under-saturated formation brine encounters CO_2 due to CO_2 dissolving in formation water, reprinted from Celia et al. (2005).

Figure 2.4 below shows two immiscible fluids, such as balanced supercritical CO_2 and brine in contact with a solid surface. Owing to the difference in cohesive forces between the molecules at the surface of each phase and the molecules in the bulk of each phase, the interface between phases emerges (Pentland et al., 2010).

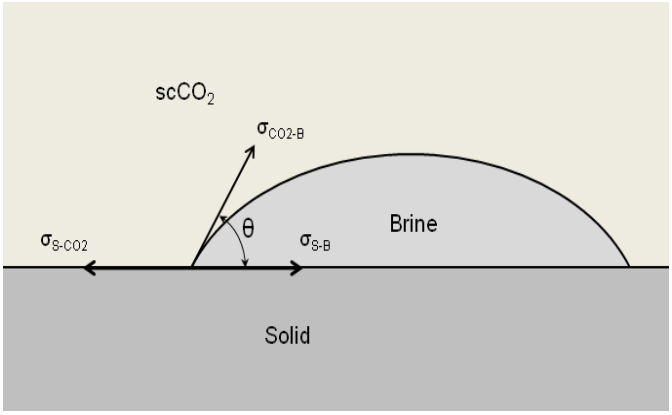

Figure 2.4: Three-phase interfacial tensions and contact angle, reprinted from Pentland et al. (2010).

Equilibrium for the system is defined by Young's **Equation 2.1**.

$$\sigma_{SC.CO_2-B} \cos\theta = \sigma_{s-SC.CO_2} - \sigma_{s-B} \tag{2.1}$$

$$\cos\theta = \frac{(\sigma_{s-SC.CO_2} - \sigma_{s-B})}{\sigma_{SC.CO_2-B}} \tag{2.2}$$

Here σ is the surface tension and subscript $SC.CO_2$ denotes supercritical carbon dioxide; *B* is the brine phase, and *S* represents the solid phase. Young's Equation also states that:

$$\theta_{s(CO_2)} - \frac{\theta s(B)}{\theta CO_2(B)} > 1 \tag{2.3}$$

Then it is completely wet with a brine phase having an angle of zero (Bear, 1988). Capillary trapping will be further discussed in more detail. To better understand capillary trapping, one must study wettability, pore structure, and capillary pressure.

2.4. Wettability

The term wettability characterizes the preference of one fluid over another to be in contact with the rock surface in a porous system with two or more fluids present (Alyafei, 2019). Generally, reservoir minerals are initially strongly water-wet. For example, in the presence of a second immiscible phase, water will preferentially spread on the rock surface. However, in oil-water systems, the wettability of the rock minerals may change over time by the adsorption of polar compounds and by the deposition of organic matter originally in the crude oil (Anderson, 1986b). It is possible to alter the wettability such that oil will spread over the rock surface in preference to water. It has been observed that water is the wetting

phase in CO_2-water siliciclastic systems (Chiquet et al., 2007; Dickson et al., 2006; Espinoza & Santamarina, 2010).

In an oil-water system, Wettability is classified into four categories: water-wet, oil-wet, neutral-wet, intermediate-wet, and mixed-wet. A system is water-wet when it prefers to be in contact with water, where the angle between a water droplet and the surface is less than 90°. Oil-wet systems prefer to be in contact with oil, forming an angle of less than 90° between an oil droplet and the surface. Neutral-wet surfaces have a similar tendency to be in contact with either fluid present in the system, therefore, forming an angle of 90° between any fluid droplet and the surface. Lastly, a mixed-wet system is water-wet in some areas and oil-wet in other regions within the same surface (Alnoush et al., 2021; Dake, 1978; Treiber & Owens, 1972).

When the non-wetting phase such as CO_2 displaces the wetting phase brine in an aquifer, the contact angle will be smaller than when brine displaces CO_2. The first case where wetting phase saturation decreases is known as drainage, while in the second case where wetting phase saturation increases is called imbibition. The difference in contact angle between these two displacement scenarios indicates the hysteresis of the system. Hysteresis refers to the fact that the state of a system – in this case, a contact angle – depends on its history, which means that the contact angle depends on the current and previous flow sequences.

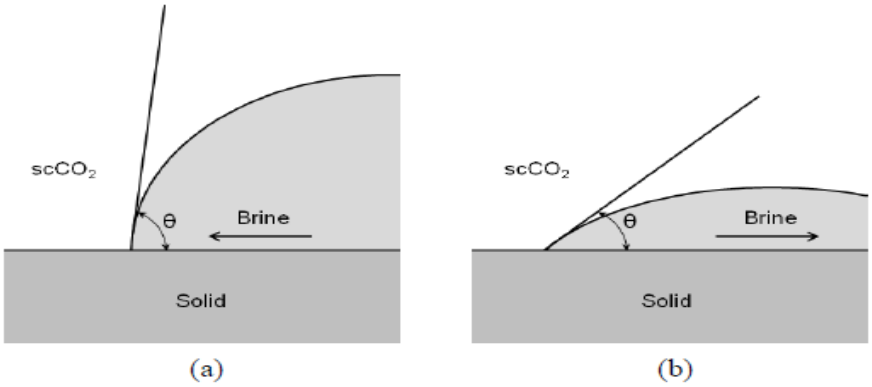

Figure 2.5: Black color represents the possible distribution of $\boldsymbol{CO_2}$*, whereas white color shows brine while grey color represents porous media. (a) Initial* $\boldsymbol{CO_2}$ *saturation after primary drainage. (b) Residual* $\boldsymbol{CO_2}$ *saturation after water-flooding, reprinted from Alyafei (2015).*

For example, the distribution of CO_2 and brine within the pore space of an immiscible displacement system. **Figure 2.6** demonstrates the CO_2 saturation before and after water flooding. As CO_2 is the non-wetting phase, it occupies the center of the pore space, and a thin layer of brine develops on the rock surface after primary drainage, as shown in **Figure 2.6a.** As the CO_2 saturation increases, it enters progressively smaller and smaller pores. **Figure 2.6b** represents the water flooded system. The term water flooding is used here alternatively with the term imbibition to denote an increase in brine saturation. The CO_2 is contained as confined droplets in the center of the pore space, surrounded by brine. The droplets of CO_2 are not extensively interconnected and are retained in place by local capillary forces. The position of the trapped droplets of non-wetting phase CO_2 depends on the extent of its initial invasion (saturation) of the pore space. The local capillary forces control how the non-wetting phase invades progressively smaller pores – and the degree of trapping.

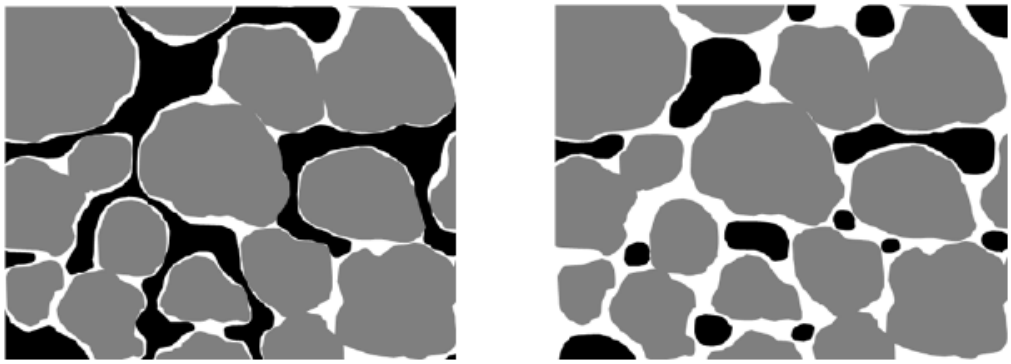

Figure 2.6: Black color represents the possible distribution of CO2, whereas white color shows brine while the grey color represents porous media. (a) Initial CO2 saturation after primary drainage. (b) Residual CO2 saturation after water-flooding, obtained from Pentland et al. (2010).

2.5. Capillary Pressure

The Laplace **Equation 2.4** makes it possible to quantify capillary pressure through an interface between two immiscible phases:

$$P_c = P_{nw} - P_w = \sigma\left(\frac{1}{r_1} + \frac{1}{r_2}\right) \tag{2.4}$$

where P_c denotes capillary pressure, P_{nw} denotes the pressure of non-wetting phase, whereas pressure of wetting phase is characterized by P_w, σ is the interfacial tension, and principal radii of curvature of the interface is denoted by r_1 and r_2.

There is an inverse correlation between capillary pressure and saturation of the wetting process, which is defined by capillary pressure curves. **Figure 2.7** indicates an immiscible mechanism where the wetting phase is water, and the non-wetting phase is CO_2, where different displacement events reflect the curves shown. The system is initially saturated with 100% water. As CO_2 reaches the system with the application of positive capillary pressure, the wetting phase saturation decreases.

This is illustrated by the drainage curve. As the water saturation decreases, the saturation of connate or irreducible water begins to approach. Applying a more significant capillary pressure at connate water saturation would not result in any more water being displaced from the system. This is the highest potential initial saturation of CO_2 as well. CO_2 will be produced from the system if water-flooded at this level, and the water saturation increases as the capillary pressure decrease.

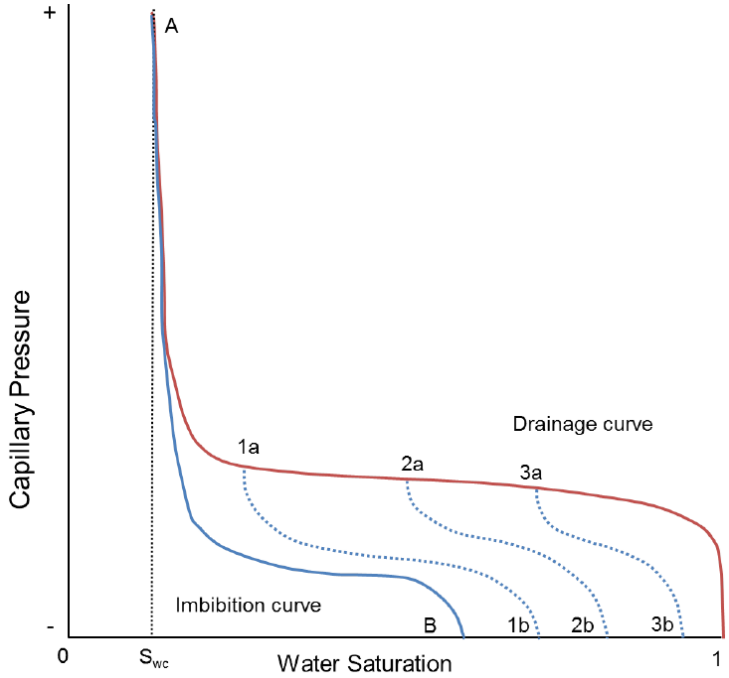

Figure 2.7: Capillary pressure curves of drainage and water-flood displacements, obtained from Alyafei (2015).

This curve ends when the capillary pressure applied during the displacement cannot produce any more CO_2. This capillary pressure may be negative, meaning that during water flooding, the water phase pressure is greater than the CO_2 phase pressure (Bear, 1988).

Saturations resulting from bounding and scanning curve displacements may characterize the hysteresis of a system. An initial CO_2 saturation and a residual CO_2 saturation is created by each set of drainage water-flood displacements. The resulting initial-residual saturation data can be traced if a number of these displacements were performed on a system, as shown in **Figure 2.8.**

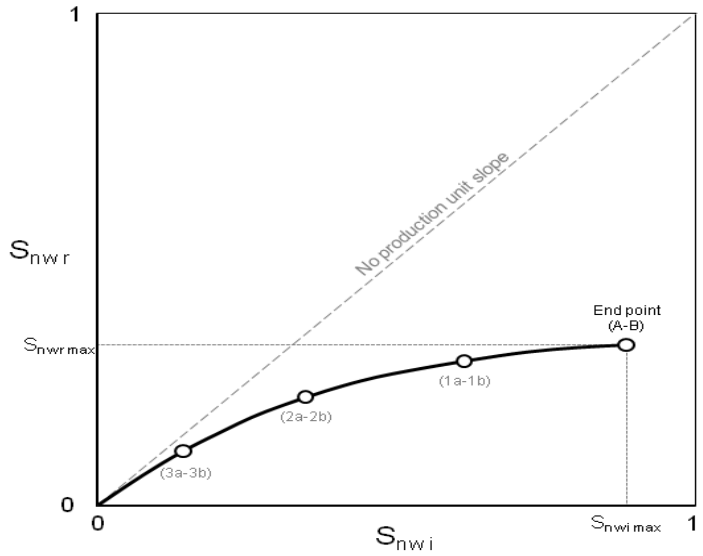

Figure 2.8: A standard capillary trapping curve for initial saturation of residual non-wetting phases, obtained from Pentland et al. (2010).

Important information about capillary trapping in a system is given by the shape of the trapping curve and the magnitude of the endpoint saturation. The area between the trapping curve and the slope line of the no-production unit indicates the amount of non-wetting phase created during the water-flooding process. The region below the trapping curve shows the quantity of non-wetting phase trapped in the system by capillary forces after water-flooding.

It is essential to understand the controls of the pore-scale on capillary trapping. A conceptual model of a porous medium is to picture it as an irregular lattice of pore

spaces bound by narrower limits, called throats, the broader gaps between grains. Imbibition is a competition between pore and throat filling, and the amount of trapping is controlled by this competition and the way it occurs (Blunt & Scher, 1995). Piston-like progress occurs when water moving from a water-filled pore or throat displaces the non-wetting phase from a neighboring pore or throat. Piston-like displacement occurs when the wetting phase moves from a pore or throat filled with wetting phase fluid to displace the non-wetting phase from neighboring pores or throats. For this phase, the threshold capillary pressure is approximate:

$$P_c = \frac{2\sigma \cos\theta}{r} \tag{2.5}$$

The radius of the pore or throat being filled is *r*. If the pores are much larger than the throats, a much lower capillary pressure is needed to fill a pore first. This ratio is known as the aspect ratio of pore diameter to throat diameter (Ra). In imbibition, the water fills elements (pores or throats) in the decreasing order of capillary pressure, filling the narrowest portions of the rock with the most substantial capillary pressures first. If the neighboring pore or throat is water-filled, it will not penetrate a throat by piston-like advance (Rabbani et al., 2019).

Snap-off is the second filling operation. Water in the corners of the pore space often flows along with wetting layers, and these layers swell during imbibition as the capillary pressure decreases. In essence, as it enters a pore, the water is impeded, but water may flow around the corners and rough surfaces and penetrate a nearby throat. This process is shown in **Figure 2.9**. The water will swell the wetting layer

until the non-wetting phase no longer contacts the wall; it becomes unstable at this point.

$$P_c = \frac{\sigma(\cos\theta - \sin\theta)}{r_t} \tag{2.6}$$

The ratio of capillary pressures of snap-off to pore filling is shown by **Equation 2.7** below:

$$\text{Ratio} = \frac{r_p}{r_t}(1 - \tan\theta) \tag{2.7}$$

Equation 2.7 shows that the ratio of capillary pressures is higher for large aspect ratios and small contact angles (strongly water-wet), favoring snap-off. Snap-off fills narrow throats, leaving the larger pores with a non-wetting process. Then the non-wetting process is trapped if all the surrounding throats are filled (Alnoush et al., 2021; Blunt & Scher, 1995; Jerauld & Salter, 1990).

Figure 2.9: Wetting Phase (blue) trapped non-wetting phase (green) by snap-off within a porous medium (grey), obtained from Alnoush et al., (2020).

Figure 2.9 illustrates three processes, in part (a) across the solid surface wetting phase related to the help of wetting layers. In part (b), capillary pressure drops during imbibition result in swelling of wetting layers. In part (c), until the throat spontaneously fills with the wetting phase, the wetting layers within the throat swell,

isolating and trapping the non-wetting phase in the previous pore (Alnoush et al., 2021).

2.6. Pore Structure: Coordination Number and Aspect Ratio

The coordination number of a porous structure links the number of connected throats to each pore. A pore that is connected to three throats has a coordination number of three. The aspect ratio quantifies how much of the pore is connected to the surrounding throats through radii comparisons. The aspect ratio can be defined in **Equation 2.8**.

$$a = \sum_{j}^{n_P} \frac{C_N r_j}{\sum_{i}^{n_t} r_{tij}} \tag{2.8}$$

Where *j* represents the pores, n_P is the total number of pores, C_N is the coordination number of pore *j*, *i* is the throat connected to pore *j*, n_t is the total number of throats connected to pore *j*, and r_{tij} is the radius of the connected throat. In other words, the aspect ratio compares the pore radius to the average radius size of the throats connected to that pore. For each system, the aspect ratio of each pore is averaged to indicate the system's aspect ratio. Studying the coordination number and the aspect ratio will allow us to select the ideal reservoirs based on their trapping capacity (Qi et al., 2010). It has been proven that the trapping capacity increases linearly with initial saturation, as compiled by S. Iglauer et al. (2009) in **Figure 2.10**. However, the literature lacks experimental comparisons of different systems with varying coordination numbers and aspect ratios with respect to trapping capacity.

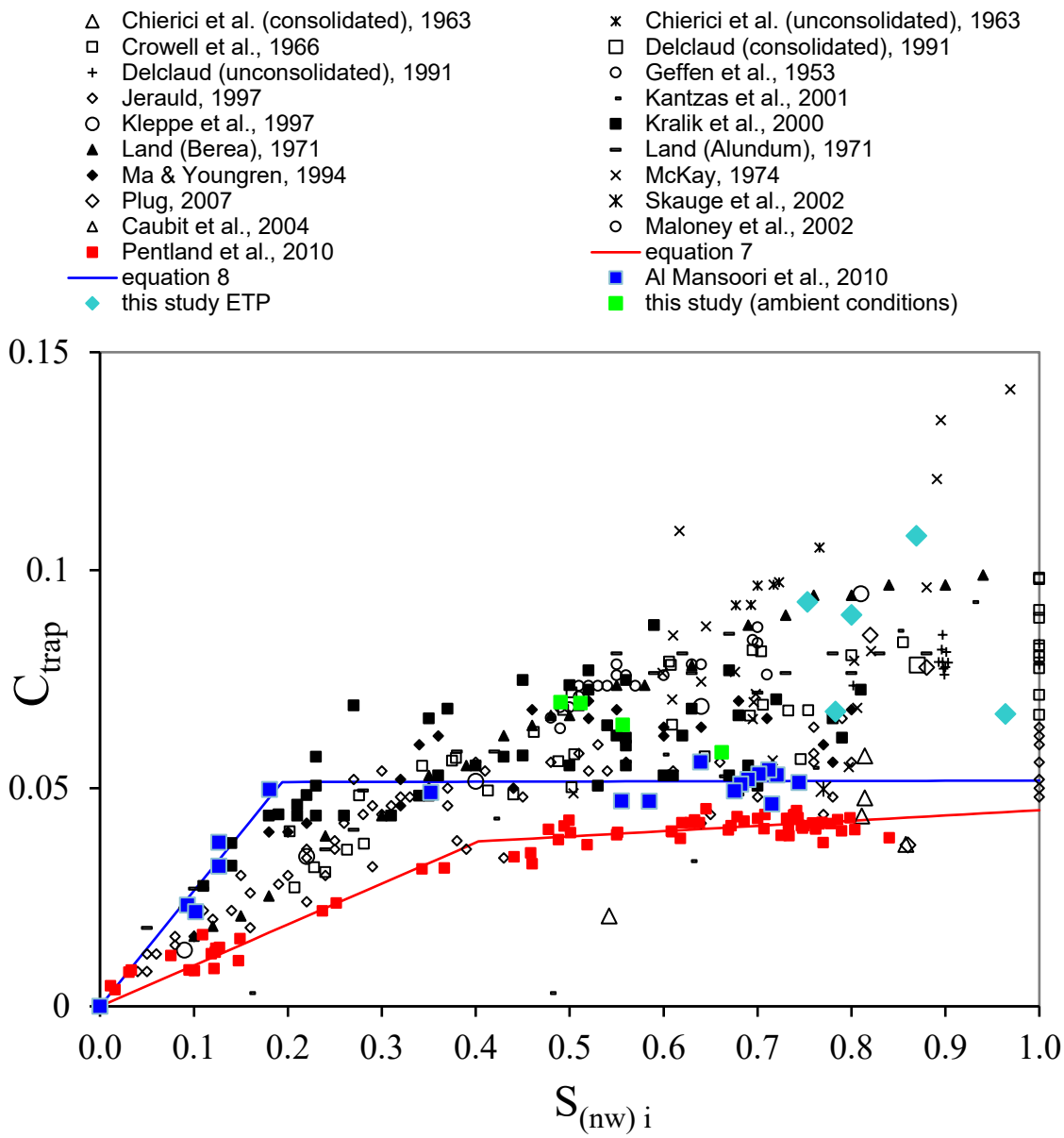

Figure 2.10: Trapping capacity as a function of the initial non-wetting phase saturation, compiled by S. Iglauer et al. (2009).

2.7. Previous Experimental Studies on Capillary Trapping

It is not only the residual saturation that is of concern for CO_2 storage and EOR applications, but the fraction of the gross rock volume comprising the trapped

phase (Holtz, 2005; Stefan iglauer et al., 2009). The capillary trapping (C_{trap}) is thus described as:

$$C_{trap} = \phi S_{(nw)r} \tag{2.9}$$

where the porosity of the system is ϕ and $S_{(nw)r}$ is the residual saturation of the non-wetting phase.

2.7.1. Capillary Trapping Capacity

2.7.1.1. Water-wet Reservoirs

Several studies reported and discussed water-wet trapping curves. These studies, shown in **Figure 2.11**, were performed under the assumption that the system was water-wet, which was demonstrated by either measuring the Amott wettability index or the spontaneous imbibition. The experiments show that the more a fluid (non-wetting phase) was injected into the reservoir, the more the reservoir trapping capacity increased (Iglauer et al., 2011). The data illustrate different fluid properties, rock types, and experimental conditions. There is considerable dispersion in the literature data comparing the capillary trapping to the residual saturation of the non-wetting phase.

However, suppose the low porosity clay-rich samples from (Suzanne et al., 2003) were removed. In that case, the trapping ability will appear to increase approximately linearly with initial saturation until an initial saturation of ~50%. There is significant dispersion beyond this, with most data suggesting a maximum capillary trapping potential of between 4% and 10%.

In water-wet reservoirs, the trapping is mainly caused by the snap-off, which means that the final residual saturation is achieved after a few pore volumes of water. In water-wet reservoirs, the snap-off will cause more oil (non-wetting phase) to be immobile if there is more water (wetting phase) in the reservoir (Alyafei, 2015). It is also observed that the increasing trend does not depend on the rock type as long as the rock is water-wet.

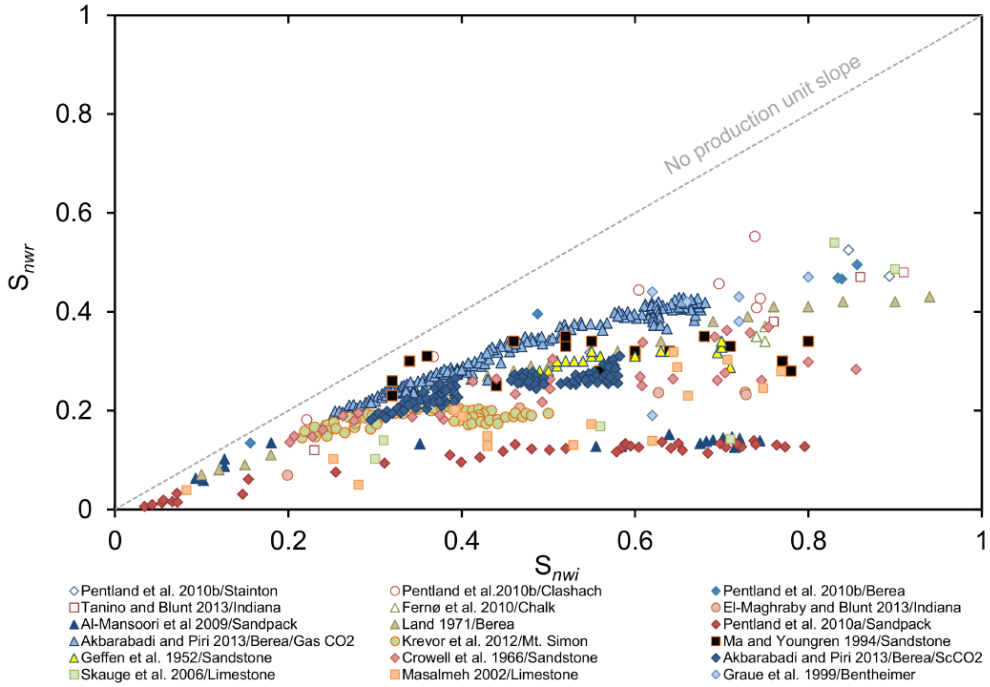

Figure 2.11: Literature database of trapping capacity as a function of initial non-wetting phase saturations for water-wet reservoirs, (Alyafei, 2015).

2.7.1.2. Altered Wettability Reservoirs

When altered-wettability reservoirs were studied, the results were different. In altered-wettability reservoirs, there was no increasing trend as the water-wet cases. This is due to the inability to reproduce the experiments. Reproducing the

wettability depends on the experimental conditions, rock type, and oil composition (Alyafei, 2015). Furthermore, **Figure 2.12** shows different rocks and wettabilities. The altered-wettability rocks illustrate less oil trapping than the water-wet rocks due to the connectivity of the oil layers in both mixed-wet and oil-wet systems, allowing the oil to flow.

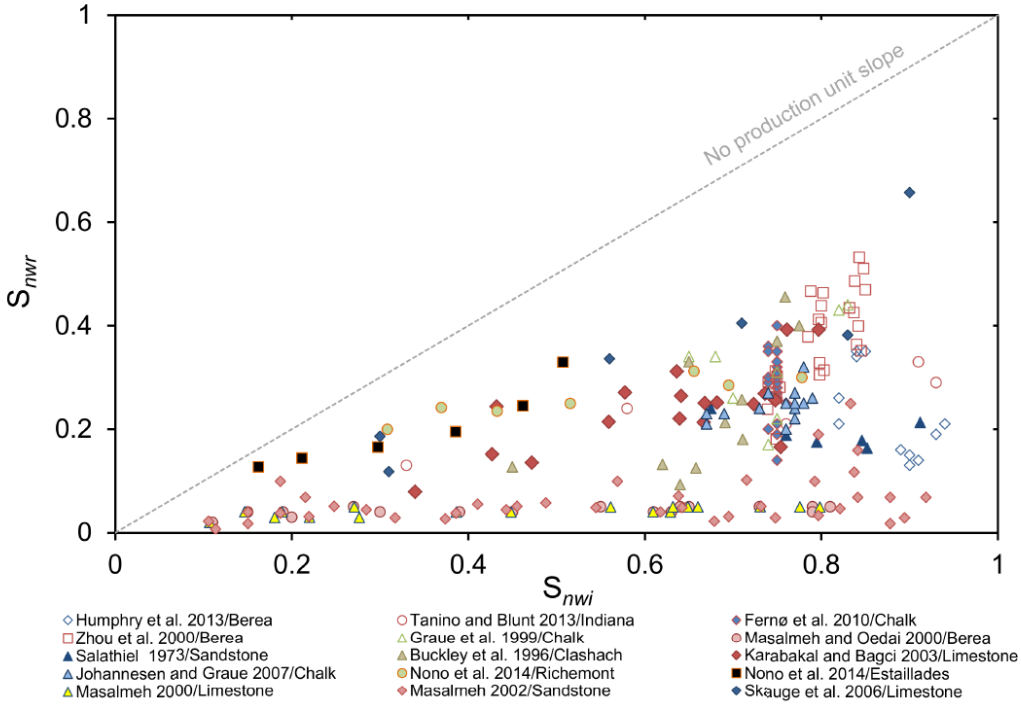

Figure 2.12: Literature database of trapping capacity as a function of initial non-wetting phase saturations for altered-wettability reservoirs, (Alyafei, 2015).

2.7.1.3. Capillary Trapping Models

To predict the pattern of trapped saturation based on the literature data, several models have been proposed. Building on the work of (Geffen et al., 1952), (Naar & Henderson, 1961), (Agarwal, 1967), and (Land, 1968) suggested a relationship between the saturation of trapped gas and the saturation of initial gas. For consolidated media, this was based on experimental results.

$$S^*_{gr} = \frac{S^*_{gi}}{1+C\,S^*_{gi}} \tag{2.10}$$

S^* is the effective saturation which is defined as $S^* = \frac{S}{1-S_{wc}}$ where S_{wci} is the connate or irreducible water saturation. Jerauld (1997) extended Land's relationship to propose a zero-slope adaptation to match the mixed-wet Prudhoe Bay oil field in Alaska with trapped gas saturation results.

$$S^*_{gr} = \frac{S^*_{gi}}{1+\left(1/S^{*max}_{gr}-1\right){S^*_{gi}}^{1/(1-S^{*max}_{gr})}} \tag{2.11}$$

Ma and Youngren (1994) suggested another adaptation of Land's relationship based on an oil-wet experimental data collection from the Kuparuk River Unit in Alaska. Ma and Youngren (1994) noticed a sharp leveling of the trapped gas saturation at higher initial gas saturation. The leveling of trapped gas saturation led to two empirically derived curve fitting parameters being added, a and b, where b=1 and a=C in the original correlation of Land:

$$S^*_{gr} = \frac{S^*_{gi}}{1+a\,(S^*_{gi})^b} \tag{2.12}$$

Data based on an artificial core (Aerolith 10, 43 percent porosity) from (Kleppe et al., 1997) did not match Land's trapping curve. To match the experiments, the following linear relation was proposed:

$$S_{gr} = \frac{S_{gi}}{S^{max}_{gi}} S^{max}_{gr} \tag{2.13}$$

The use of pore-scale modeling is another approach to the prediction of trapped saturation. Spiteri et al. (2008) used a pore-network model developed by Valvatne and Blunt (2004) to predict the trapped saturation as a function of initial saturation

and average contact angle. Their model matched the residual saturation measured on Berea sandstone by (Oak et al., 1990). As a quadratic function of initial saturation, they matched the simulated pattern of trapped saturation for a given contact angle distribution:

$$S_{or} = \propto S_{oi} - \beta_s {S^2}_{oi} \tag{2.14}$$

Where $\propto$ and β_s are contact-angle dependent coefficients. These two widely used models, Land (1968) and Spiteri et al. (2008), are limited since they require capillary data for them to work. The fitting constant in the two models is not based on inputs other than the initial and residual saturations of the non-wetting phase. The two fitting models do not implement the effect of the pore structure on the capillary trapping capacity. Therefore, there needs to be a capillary trapping estimation method that utilizes the pore structure of the reservoir.

3. THESIS PROBLEM AND OBJECTIVES

This work aims to study the relationship between capillary trapping and residual saturation in an air-water system. Due to the lack of experimental investigations on trapping capacity in terms of varying coordination number and aspect ratio as discussed in the literature review, and because of their importance, this work provides a guiding equation for capillary curve prediction based on the pore structure of the system. Predicting the capillary trapping capacity based on the pore structure or pore geometry would be essential to the industry. The findings of this thesis could be coupled with the literature's results that link capillary trapping to the factors affecting it, such as wettability, capillary pressure, and capillary number. Moreover, the outcomes of this experiment will provide insight into the selection process of carbon dioxide sequestering processes based on the estimated trapping capacity of the reservoir.

The experiments were conducted through various 3D printed pore-network models, with varying pore structures, where the distribution and pattern of the trapped fluid in the system will be examined. The results of this work will expand the understanding of two-phase flow in porous media. This work will have the following specific objectives:

1- Compare the capillary trapping curves and trapping capacities of four water-wet models, with varying average coordination numbers and average aspect ratios.
2- Formulate an empirical relationship to relate average coordination number and average aspect ratio to capillary trapping.
3- Conclude the effect of coordination number and aspect ratio and how these parameters can improve the selection process of storage reservoirs.

4.1.1. Pore Network Modeling and Printing

Four 3D printed models, shown in **Figure 4.1**, were used to simulate four pore network models to investigate the effect of the average coordination number and aspect ratio on the trapping curves. The four model designs were selected from Alyafei et al. (2020), which investigated and modeled binary images from ortho slices or synthetic systems designed using Adobe illustrator. These four models (A, B, C, and D) were selected based on the homogeneity or heterogeneity of the system.

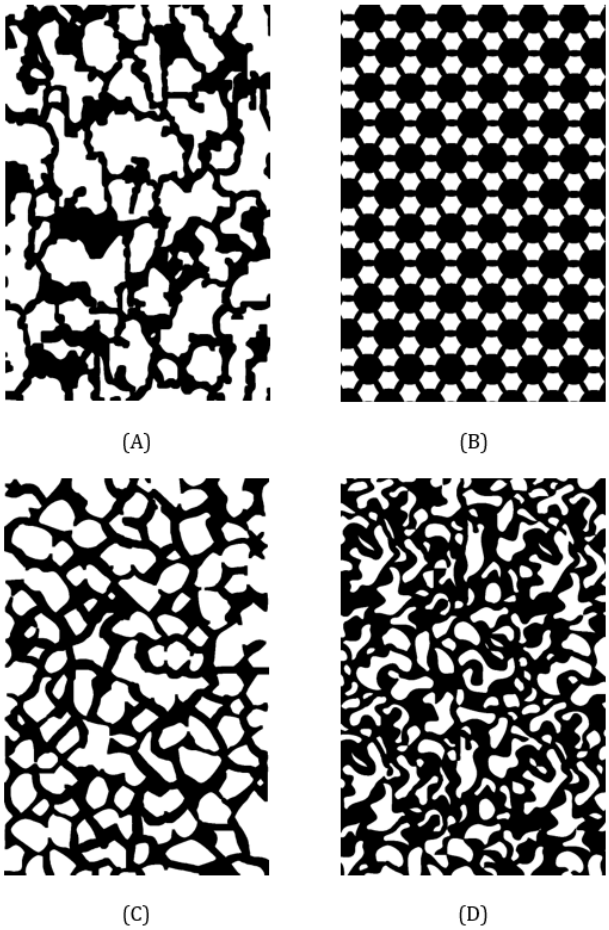

Figure 4.1: The designs of the four studied pore models, obtained from Alyafei et al. (2020).

These models were designed using a MATLAB tool developed in Texas A&M University at Qatar through image processing, micromodel construction, and model post-processing. Filters such as the Gaussian, non-local mean, and median were applied to reduce the noise from the images (Alyafei et al., 2020). After the segmentation, morphological image operations were applied to remove isolated pores, which is an essential step before printing the model. Then, the pore network models were created with the crucial micromodel components. The model files were then printed using a transparent resin and the ANYCUBIC Mono X 3D printer. The printing settings are shown in **Table 4.1** below.

Table 4.1: Summary of the 3D printing settings.

Layer Thickness (mm)	0.05
Normal Exposure Time (s)	2
Bottom Exposure Time (s)	40
Bottom Layers	6
Z Lift Speed (mm/s)	2
Z List Distance (mm)	8

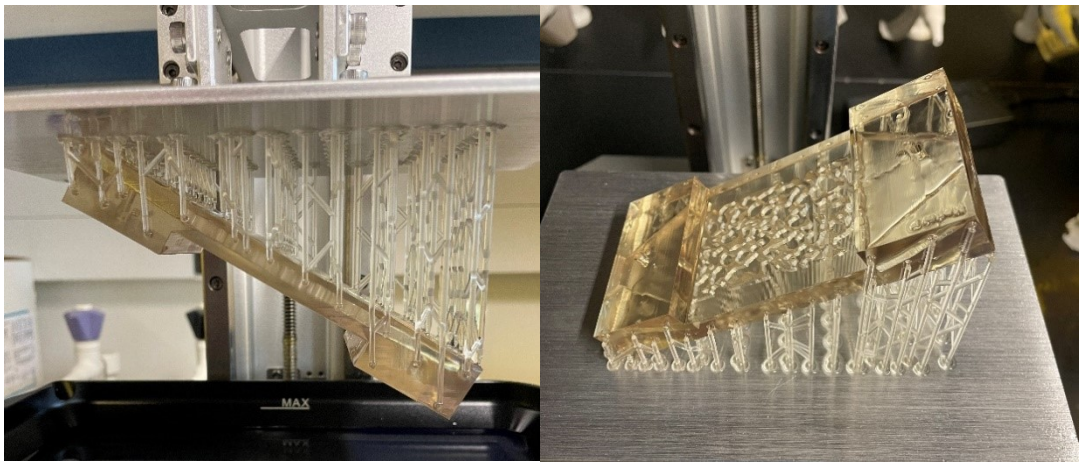

Figure 4.2: Model A before curing and polishing.

The printed pore network models were cleaned with alcohol, cured using UV light, and polished to increase transparency. The model dimensions are shown in **Figure**

4.3. Comparing the right image of **Figure 4.2** to **Figure 4.3**, the inlet of the model is on the left, the outlet on the right, and the dimensions are the same for all models.

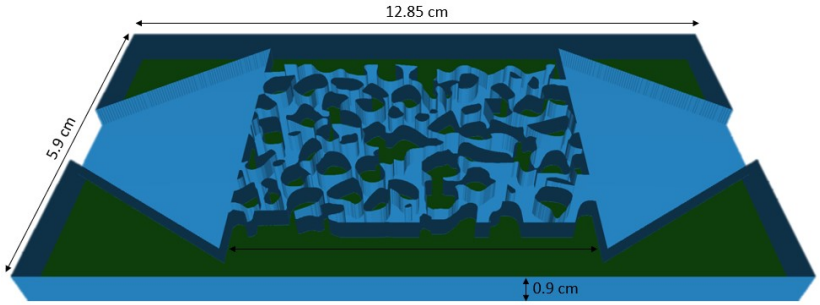

Figure 4.3: General model dimensions applied to all four pore network models.

The contact angle between a water droplet and the 3D printing resin was measured to verify the wettability of the system. Contact angle measurements were conducted using a goniometer manufactured by rame-hart (model 50) with an upgraded camera connected to the DROPimage advanced sessile drop optical analysis and contact angle software. Contact angle measurements were taken at three different times, as shown in **Figure 4.4**, with three minutes between each measurement to allow the water droplet to spread on the resin surface. The right, left, and mean angle measurements are shown in **Table 4.2**.

Figure 4.4: The three contact angle measurements of the same droplet, with 3-minute time intervals.

Table 4.2: Detailed contact angle measurement of the droplet, at three-time steps.

Measurement	Left Angle	Right Angle	Mean Angle
1	33.2˚	32.0˚	32.6˚
2	26.3˚	21.1˚	23.7˚
3	21.4˚	18.1˚	19.8˚

The resin material was confirmed to be strongly water-wet ($\theta < 45^{\circ}$) since the average of the contact angle mean values is 25.4°, which indicated a preference of the resin surface to be in contact with water in the presence of air. It is important to note that the contact angle measurement was done on a non-polished 3D printed resin since the inside pores of the printed systems were not polished either.

4.1.2. Calculation of the Average Coordination Number and Average Aspect Ratio

To calculate the average coordination number and the aspect ratio, Avizo 9.1 was used to generate a pore network model. The same image in **Figure 4.1** of each model was duplicated 98 times to give depth to the model and match the model dimensions shown in **Figure 4.3**. After volume rendering, auto thresholding, axis connectivity, and volume fraction creation, the interconnected pores that provide the effective porosity were visualized and calculated.

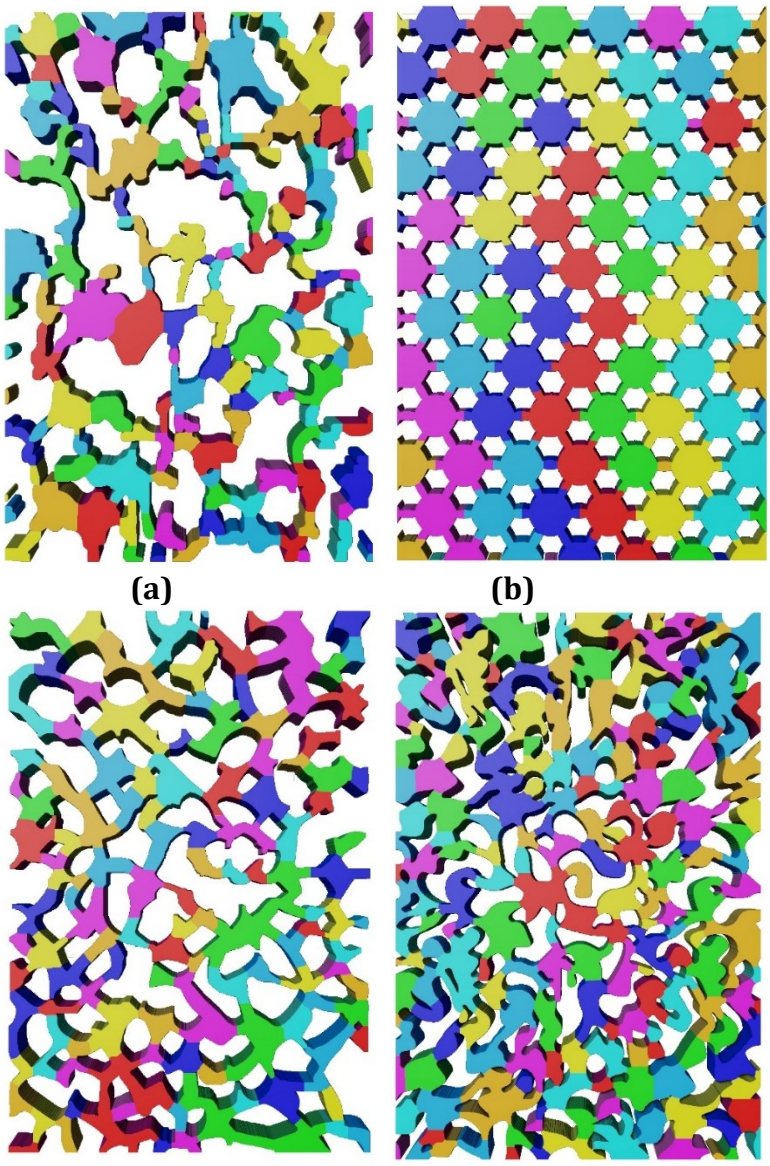

Figure 4.5: The 3D view of the connected pores in (a) model A, (b) model B, (c) model C, and (d) model D, visualized on Avizo 9.1.

These steps were done on Avizo 9.1, following the Avizo 9.1 network modeling manual. Then the pore network model was generated based on the throat and pore sizes on the Avizo 9.1 software, as shown in **Figure 4.6**.

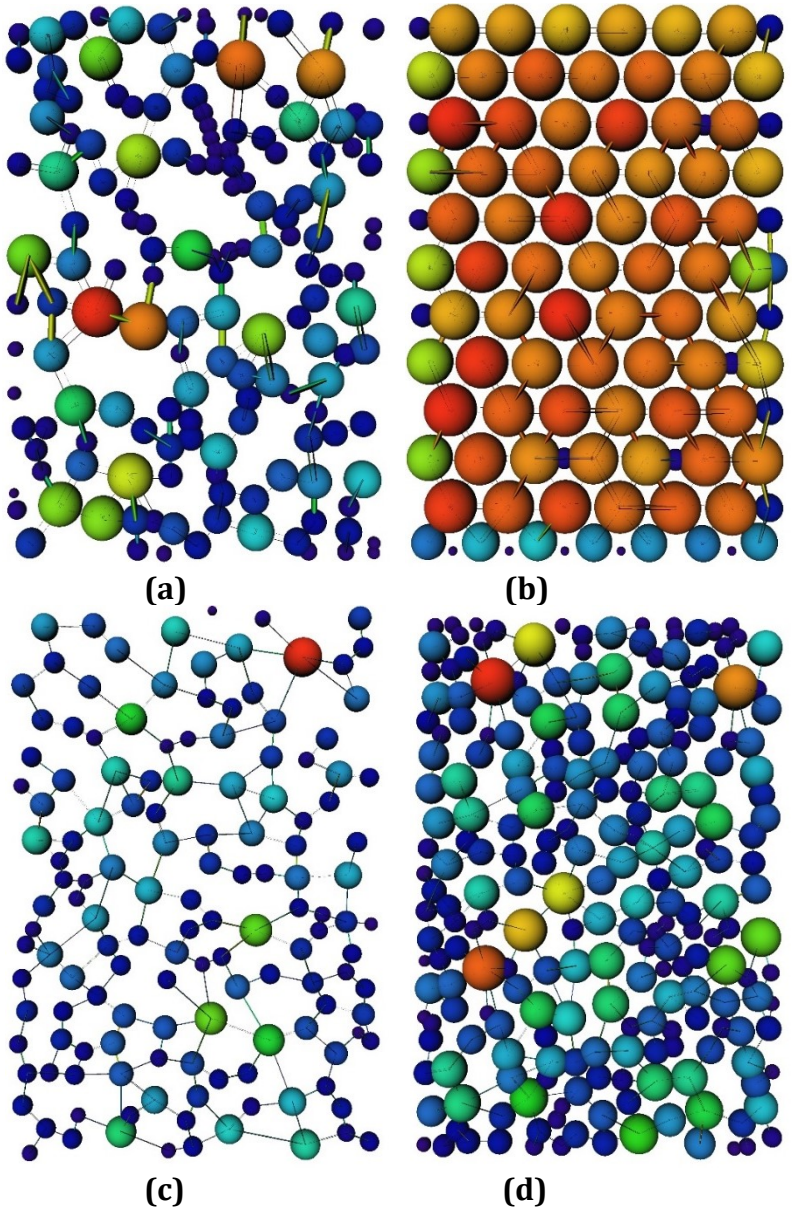

Figure 4.6: The pores and pore network models of (a) model A, (b) model B, (c) model C, and (d) model D visualized on Avizo 9.1.

The Avizo 9.1 software provided the average coordination number and the parameters needed to calculate the average aspect ratio for each model, as shown in **Table 4.3**.

Table 4.3: Summary of the resulted average aspect ratio, average coordination number, number of pores, and number of throats using Avizo 9.1.

Model	Porosity [-]	Number of Pores [-]	Number of Throats [-]	Average Coordination Number [-]	Average Aspect Ratio [-]
A	0.42	154	179	2.30	1.51
B	0.63	99	215	4.40	2.47
C	0.46	142	196	2.80	1.59
D	0.61	225	346	3.10	1.66

Equation 4.1 shows how the average aspect ratio was obtained based on the sum of the throat radii connected to each pore.

$$a = \sum_{j}^{n_P} \frac{C_N r_j}{\sum_{i}^{n_t} r_{tij}} \tag{4.1}$$

Where j is the pore, C_N is the coordination number of that pore j, n_P is the total number of pores in the system, n_t is the total number of throats connected to that pore, r_{tij} represents the throat's radius connected to the pore, and *i* represents the throat connected to pore j. Furthermore, two-pore structure parameter extraction methods were used to calculate the average coordination number and the average aspect ratio. The two models, Dong and Blunt (2009) and Raeini et al. (2017), rely on different extraction and calculation methods.

Dong and Blunt (2009) use a modified maximal ball algorithm, based on the work of Silin and Patzek (2006), to scan micro-computerized-tomography images to construct a 3D pore network. The modified maximal ball algorithm extracts simplified networks of the pores and throats of a system. The pores in this network model are represented by the largest sphere size that fits in the pore void, and the

throats are represented by chains of smaller-sized spheres connected to the pores, as shown in **Figure 4.7**.

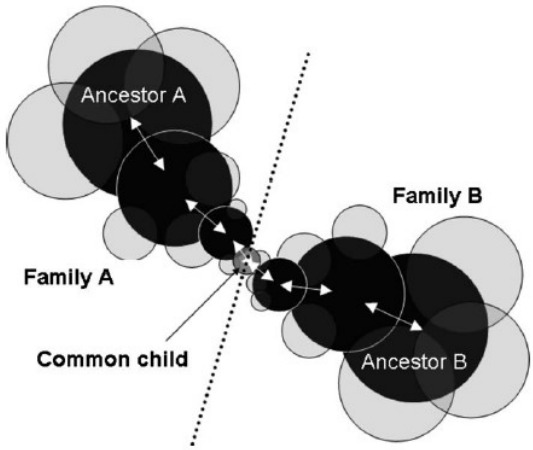

Figure 4.7: Schematic of the pore and throats spheres, obtained from Dong and Blunt (2009).

The extracted results for each of the four models using Dong and Blunt (2009) network model are shown in **Table 4.4**.

Table 4.4: Summary of the resulted average aspect ratio, average coordination number, number of pores, and number of throats using Dong and Blunt (2009) network model.

Model	Number of Pores [-]	Number of Throats [-]	Average Coordination Number [-]	Average Aspect Ratio [-]
A	130	181	2.61	1.58
B	108	279	4.94	2.98
C	167	284	3.25	1.43
D	123	173	2.68	1.57

Raeini et al. (2017) use a generalized network that discretizes the generated surface from a medial-axis 3D image transformation. The discretization splits the void into separate pores. Then, each pore is further divided into sub-elements, which are the half-throat connections, divided into corners based on the medial axis axial plane

analysis. The extracted results for each of the four models using Raeini et al. (2017) network model are shown in **Table 4.5**.

Table 4.5: Summary of the resulted average aspect ratio, average coordination number, number of pores, and number of throats using Raeini et al. (2017) network model.

Model	Number of Pores [-]	Number of Throats [-]	Average Coordination Number [-]	Average Aspect Ratio [-]
A	319	706	4.29	1.07
B	134	334	4.69	2.44
C	359	988	5.37	1.04
D	275	619	4.36	1.08

It was observed that both Avizo 9.1 and Dong and Blunt (2009) network models have much closer average coordination number and average aspect ratio values due to the close number of pores and throats observed by the networks. On the contrary, the Raeini et al. (2017) network model calculated more pores and throats, leading to higher average coordination number and average aspect ratio values. The overestimation of pores and throats is further discussed in the results and discussion section.

4.1.3. Performing the Experiments

Water was injected to fully saturate the 3D system with a 50 ml CONTEC model SP500 syringe pump. The fluid, water, was observed with a Canon A7-3 camera with a FE 2.8/50 Macro lens. Water was colored in blue to increase the contrast in the imaging. Drainage and imbibition were visualized using a time series imaging, which quantified the initial and residual gas saturation. First, the air was injected into the fully water-saturated system with a randomized volume, after which the first image

of the system was taken. Then, several pore volumes of water were injected into the system to sweep the air out, leaving the irreducible gas saturation trapped in the system. The second image of the system pore network is taken after water flooding to show the trapped air, as shown in **Figure 4.8**.

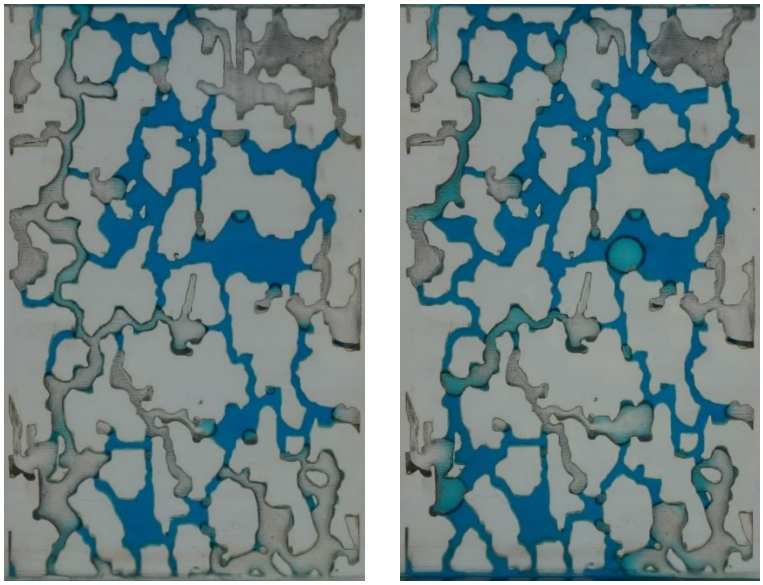

Figure 4.8: Two images showing two steps to calculate a point on the saturation curve. The first image on the left represents the initial gas saturation, while the second image on the right represents the residual gas saturation.

This process was repeated multiple times for each of the four systems. A total number of 160 images were taken, which later resulted in 80 data points in total. The pictures taken were analyzed using ImageJ.

4.1.4. Image Processing and Fluid Saturations

The porosity value of each model was calculated through ImageJ and the model picture obtained from Alyafei et al. (2020), as shown in **Figure 4.9**, where the red part is the connected porosity, and the white part shows the grains.

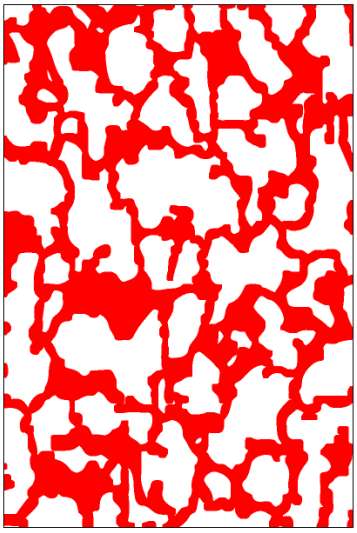

Figure 4.9: Model A calculated porosity using ImageJ. Interconnected pores are highlighted in red, and the grains are in white.

ImageJ and GIMP software were used simultaneously to calculate the percentage of water at each point. ImageJ was used to detect the fluid contrast and estimate the percentages of present fluids. These percentages were later used to calculate the initial and residual gas saturation. GIMP is an open-source image editing software that was used in this study to posterize pictures. Posterizing was applied on the obtained images to allow ImageJ to detect the fluid percentages more easily.

Every taken image was first split into color channels, using ImageJ, which provided an 8-bit image with high contrast, as shown in part (a) of **Figure 4.10**. Color separation was done before the posterizing step on GIMP, which increased the accuracy of fluid percentage estimation. Posterizing reduces the gradual color change in an image, making the colors more distinct. A posterized image of model A is shown in part (b) of **Figure 4.10**. These two steps were done before the fluid

percentage calculation, which was also done using ImageJ, shown in part (c) of **Figure 4.10**.

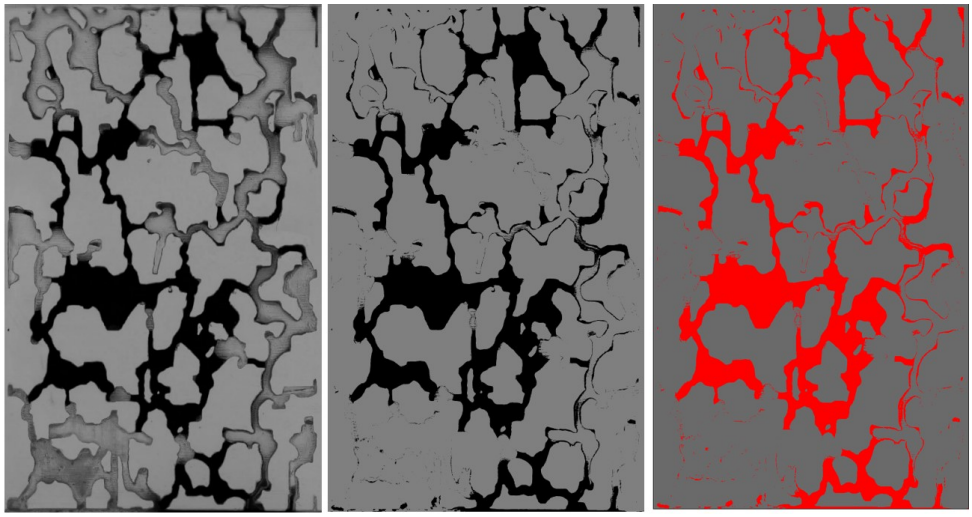

(a) **(b)** **(c)**

Figure 4.10: (a) Model A image after splitting the colors to process the image easier. (b) A posterized image of a time-step image of model A using GIMP. (c) The fluid percentage detection using ImageJ.

An upper and a lower threshold were also considered in the fluid fraction calculation to account for image processing errors. ImageJ was also used for the upper and lower threshold, without the posterizing step. The posterizing step is considered the average that lies between the thresholds. After obtaining the image in **Figure 4.10a**, the thresholds in estimating the water fraction were calculated, as shown in **Figure 4.11**. The lower and upper water fraction limit of each picture was used to calculate the standard deviation of each point in the capillary trapping curve.

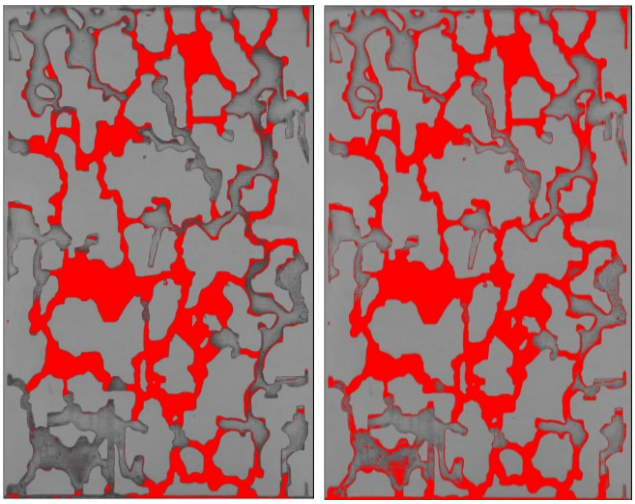

(a) **(b)**

Figure 4.11: The (a) lower and (b) upper thresholds of the water (in red) fraction calculation.

After calculating the fluid (water) percentages, the initial and residual water saturations were calculated through **Equations 4.2** and **4.3**, where the initial and residual gas saturations are calculated through **Equations 4.4** and **4.5**.

$$S_{wi} = \frac{(Water\ Percentage)_i}{Porosity} \tag{4.2}$$

$$S_{wr} = \frac{(Water\ Percentage)_{i+1}}{Porosity} \tag{4.3}$$

$$S_{gi} = 1 - S_{wi} \tag{4.4}$$

$$S_{gr} = 1 - S_{gr} \tag{4.5}$$

Where S_{wi} is the initial water saturation, S_{wr} is the residual water saturation, S_{gi} is the initial gas saturation, and S_{gr} is the residual gas saturation.

5. RESULTS

The average coordination number indicates the average number of throats connected to a pore in the system, which influences the effective porosity and permeability of the system (Krevor et al., 2015). In this work, the average coordination number of each model was taken as a representative of the Avizo 9.1 pore network model; however, one can look at the probability density function of the coordination number of each system to compare them. Similarly, the average aspect ratio for each model was taken as a representative from the Avizo 9.1 network model in the comparisons and analysis. It was observed that the average coordination number and the average aspect ratio obtained from Avizo 9.1 of all the models were close to the most occurring value, except for the average coordination number of model B, which was approximately 4.5, compared to 6 that had the highest probability density. In this case, because model B is a homogenous system, as shown in **Figure 5.1**, most of the pores were connected to six throats. However, the pores on the sides of the models were connected to fewer throats, which brought the coordination number down. Therefore, the average coordination number of model B was considered instead of the most probable value since it is affected by the sides of the models that reduced its average coordination number from 6.0 to 4.4.

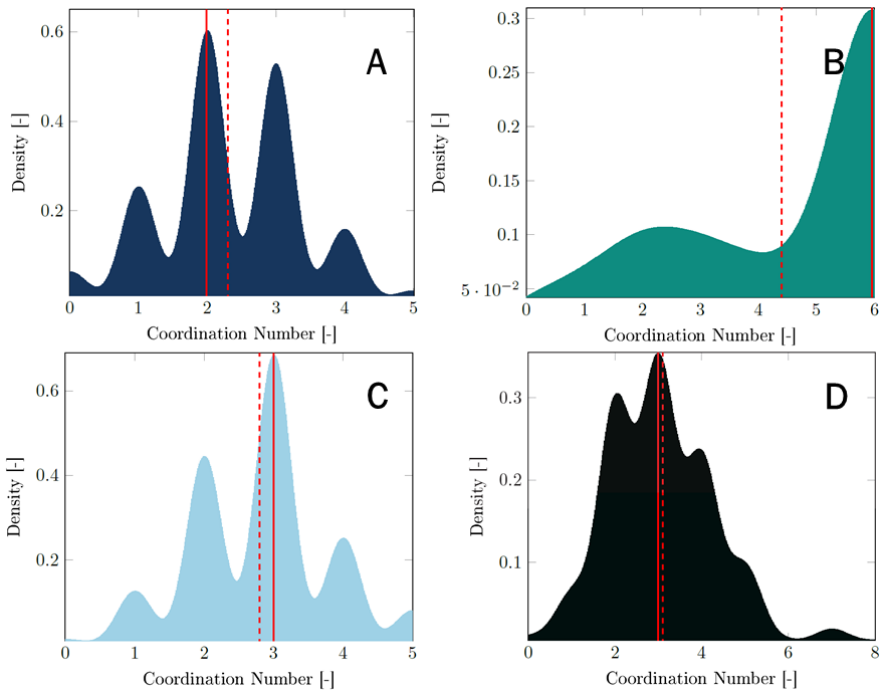

Figure 5.1: Coordination number probability density functions of models A-D from Avizo 9.1. The solid red line is the most probable value, and the dashed red line is the average value.

Similarly, the average aspect ratio for each model was taken as a representative of the Avizo 9.1 pore network model for comparisons and analysis. **Figure 5.2** below shows the average aspect ratio probability density functions of the four models, calculated using the Avizo 9.1 pore network model outcomes.

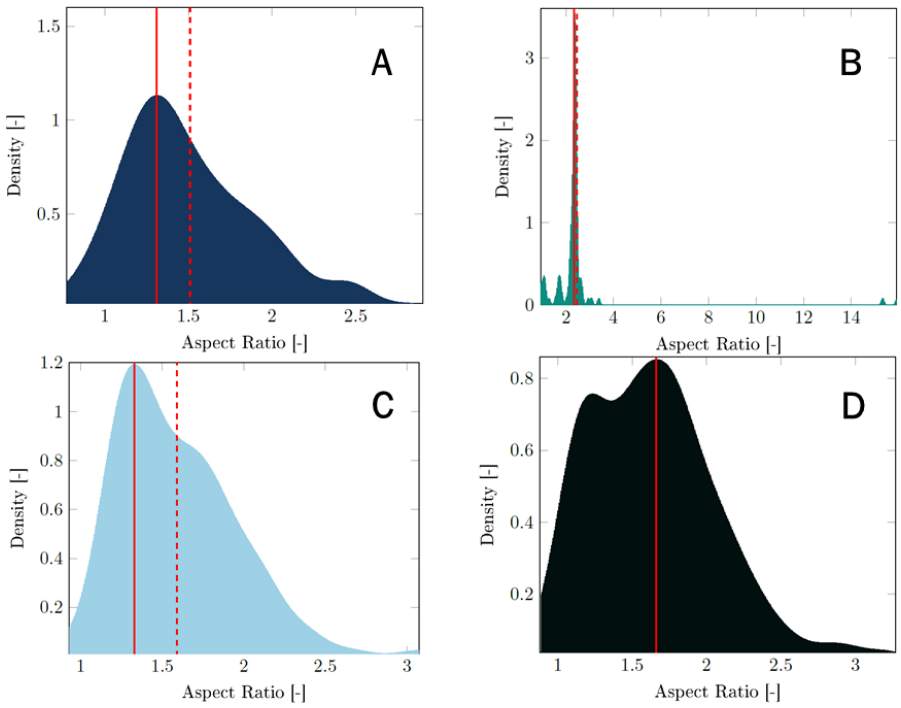

Figure 5.2 Aspect ratio probability density functions of models A-D from Avizo 9.1. The solid red line is the most probable value, and the dashed red line is the average value.

To further analyze the differences among Avizo 9.1, Dong and Blunt (2009), and Raeini et al. (2017) in the calculation and distribution of the system coordination number and the aspect ratio, the coordination number and the aspect ratio probability density functions of the latter two methods were also plotted. **Figure 5.3** shows the coordination number probability density function of all the models using the Dong and Blunt (2009) network extraction model.

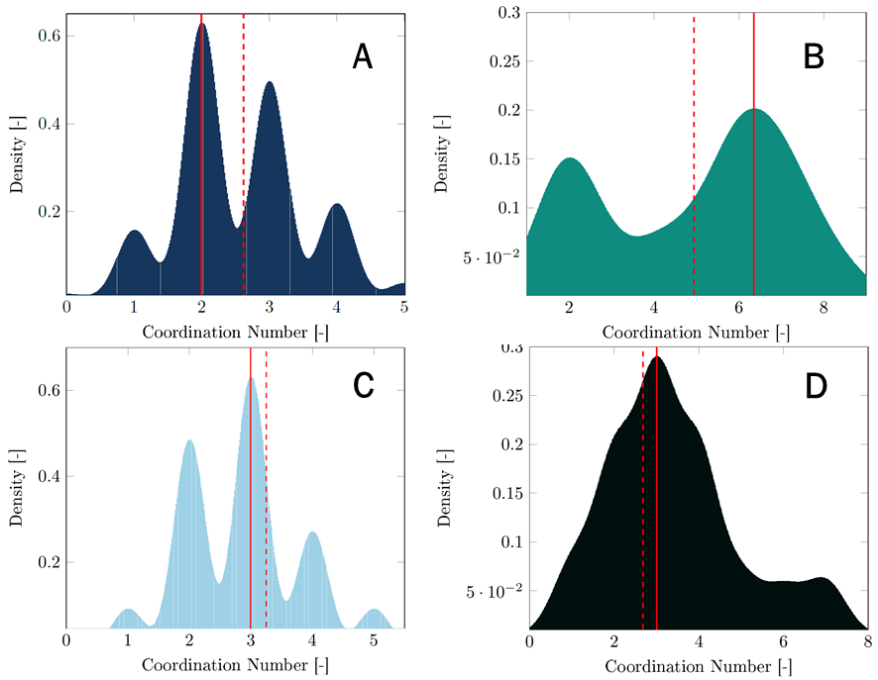

Figure 5.3: Coordination number probability density functions of models A-D from Dong and Blunt (2009). The solid red line is the most probable value, and the dashed red line is the average value.

It was observed that, unlike the Avizo 9.1 outputs, the difference between the average and the most probable value coordination number values was noticeable in all the models, except for model C as shown in **Figure 5.3**. However, the average coordination number values of the four models from Dong and Blunt (2009) network model agree with the Avizo 9.1 model. The same was observed for the aspect ratio probability density function of the same network, when compared to the Avizo 9.1 pore network calculations, the average aspect ratio values of each system were consistent. However, the most probable aspect ratio value was different and, unlike the outcomes from Avizo 9.1, not as close to the average aspect ratio, as shown in **Figure 5.4** below, which is due to the definition of pores and throats in this method.

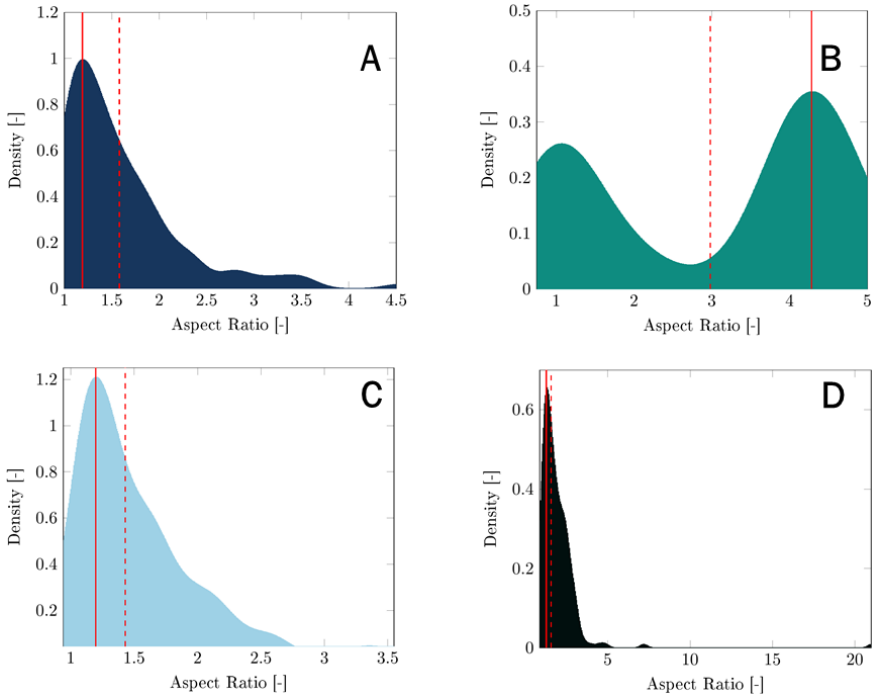

Figure 5.4: Aspect ratio probability density functions of models A-D from Dong and Blunt (2009). The solid red line is the most probable value, and the dashed red line is the average value.

On the contrary, the pore network model outcomes obtained from Raeini et al. (2017) were different due to the difference in calculation of the number of pores and throats in the model, as shown in **Table 4.5**. This difference is due to the definition of pores and throats in the maximal axis method. This method's definition of pores and throats resulted in the average coordination number being overvalued compared to the first two network models discussed earlier.

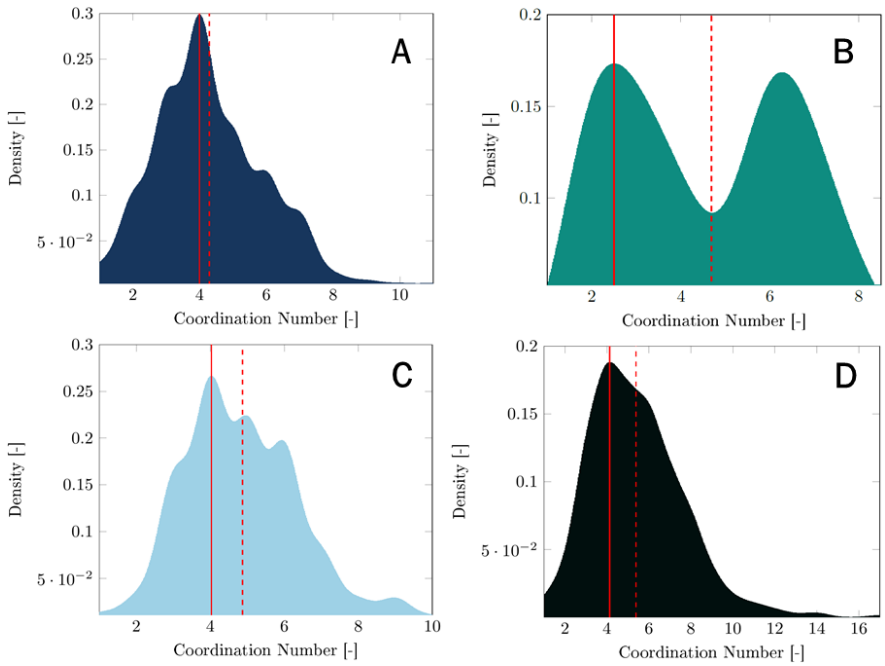

Figure 5.5: Coordination number probability density functions of models A-D from Raeini et al. (2017). The solid red line is the most probable value, and the dashed red line is the average value.

Furthermore, the overestimation of the number of throats compared to the number of pores in the Raeini et al. (2017) network model resulted in underestimating the average aspect ratio of the system compared to the two aforementioned network models. **Figure 5.6** shows how the probability density function of models A, C, and D have a spike and a most probable aspect ratio value of approximately 1, indicating the inability to distinguish between pores and throats in the medial axis extraction method.

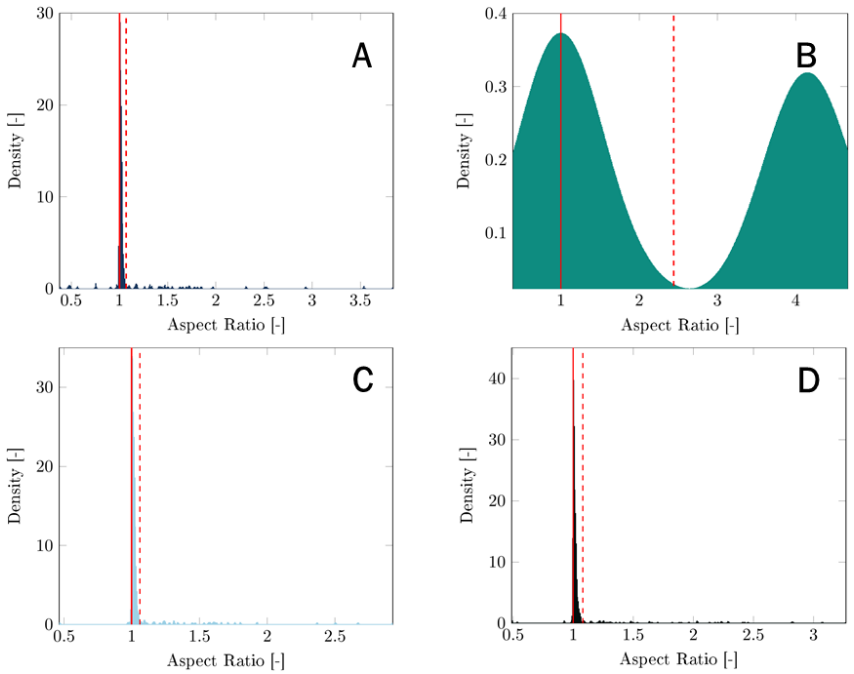

Figure 5.6: Aspect ratio probability density functions of models A-D from Raeini et al. (2017). The solid red line is the most probable value, and the dashed red line is the average value.

After obtaining all the data from the 160 processed images, they were all grouped in **Figure 5.7**. The experimental data agree with the literature gathered by S. Iglauer et al. (2009) and show a clear trend between the non-wetting phase (gas) and the wetting phase (water).

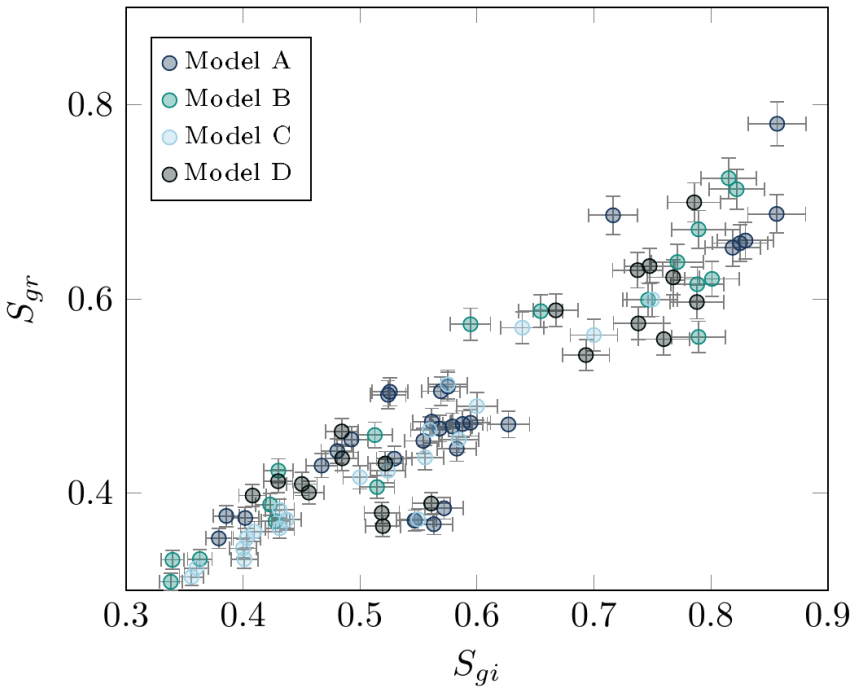

Figure 5.7: Experimental capillary trapping data of the four porous media models combined.

The average value of the residual gas saturation over the initial gas saturation of each of the four models was plotted against each model's average aspect ratio and average coordination number.

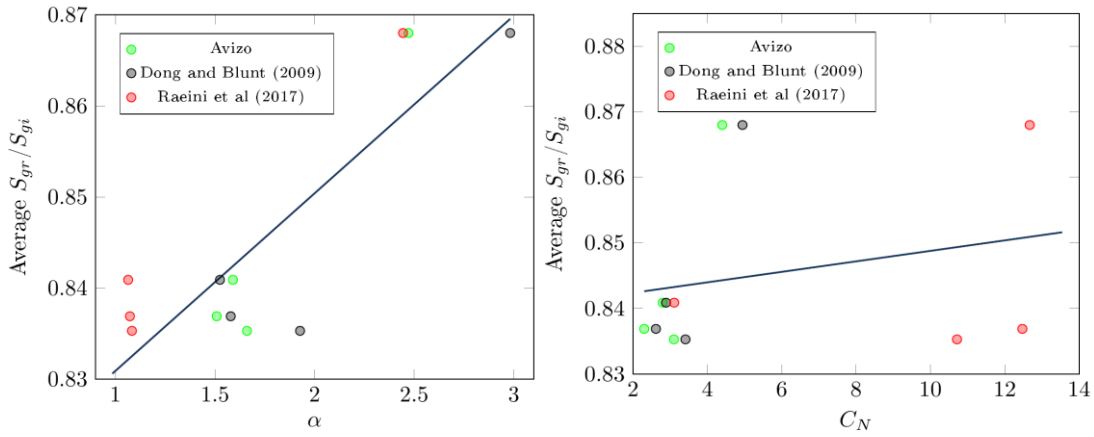

Figure 5.8: The trapping capacity, represented in the average residual saturation over the average initial saturation of each model, as a function of the average aspect ratio and the average coordination number obtained from the three pore network models.

The general trend observed is that both the average coordination number and the average aspect ratio have a direct correlation with the trapping capacity. A higher average aspect ratio value indicates that the average size of the pores is higher than the average-sized of the throats connected to them, which increases the snap-off effect. When the snap-off effect is increased, the non-wetting phase is trapped at the pores and would require a much higher capillary pressure to leave the pore to the smaller throats. Similarly, a higher average coordination number indicates more throats are connected to each pore, independent of the size of the throats, which makes it easier for the non-wetting phase to have a continuous flow and reduce trapping. However, **Figure 5.8** above shows that the increase in trapping with the rise of the coordination number is due to how linked the average coordination number and the average aspect ratio are. A single relatively large pore could be connected to five throats, with small radii, which makes the aspect ratio of that pore high, indicating better trapping. The average coordination number is an indicator of the pore structure; however, it can be considered a weak indicator on its own. Therefore, a new parameter is introduced, which combines the average aspect ratio and the average coordination number. The pore structure β is the ratio between the average aspect ratio (α) and the average coordination number (C_N), where $\beta = \frac{\alpha}{C_N}$.

Table 5.1 shows each model's pore structure parameter value based on the three extraction methods mentioned earlier. Hence, the effect of the pore structure parameter was highlighted in **Figure 5.9**. It was observed from the regression line of

each model that the higher the pore structure parameter is, the higher the slope of the regression line was. Higher slope values indicate that trapping becomes more effective at higher initial saturations of the non-wetting phase (gas) with a higher pore structure parameter.

Table 5.1: The calculated pore structure parameters obtained from the three network models.

Method	β_A [-]	β_B [-]	β_C [-]	β_D [-]
Avizo 9.1	0.657	0.563	0.568	0.536
Dong and Blunt (2009)	0.604	0.603	0.441	0.586
Raeini et al. (2017)	0.250	0.521	0.194	0.249

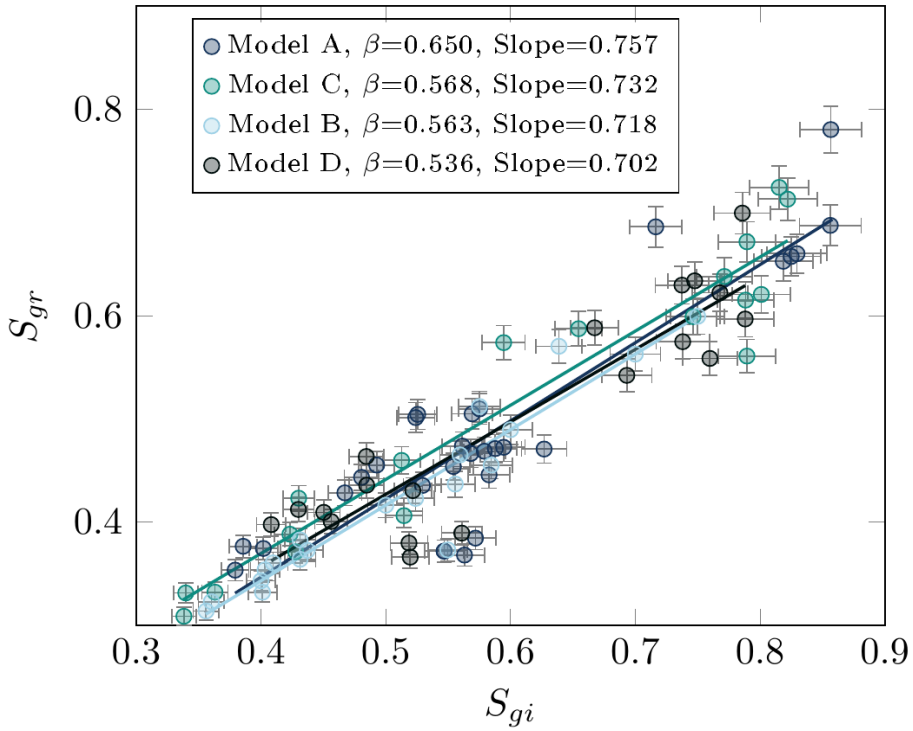

Figure 5.9: The capillary trapping data, like Figure 5.7, but with highlighting the different models and their pore structure parameters. The equations of the regression line show that models with a higher pore structure parameter have a better trapping capacity at higher initial gas saturation.

The pore structure parameter was then introduced to the capillary trapping data, as shown in **Figure 5.10**. Since the relationship between the average aspect ratio and

trapping is directly proportional, and the average coordination number is indirectly proportional, the pore structure parameter was multiplied by the initial gas saturation.

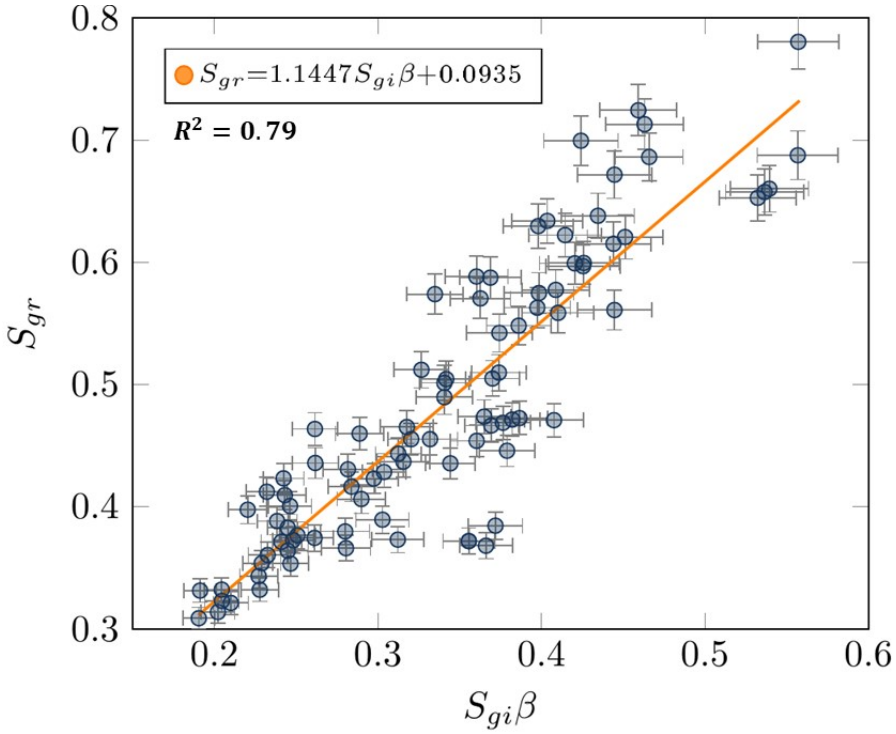

Figure 5.10: The capillary trapping data after introducing the pore structure parameter, which will be used as a model to estimate future trapping capacities of water-wet systems.

From the linear regression of the data, the following empirical equation was obtained, with an excellent coefficient of determination of 0.79. This empirical equation can estimate the residual saturation of the non-wetting phase at a given initial saturation using the pore structure parameter.

$$S_{gr(nw_r)} = 1.1447 * S_{gi(nw_i)}\beta + 0.0935 \quad (5.1)$$

The formulated equation only requires the pore structure parameter of a system to estimate its trapping curve. Therefore, it is essential to compare different pore structures and pore network extraction methods through the obtained equation in this analysis, as shown in **Figure 5.11**. The previously mentioned pore network extraction methods, Avizo 9.1, Dong and Blunt (2009), and Raeini et al. (2017), were considered for the comparison.

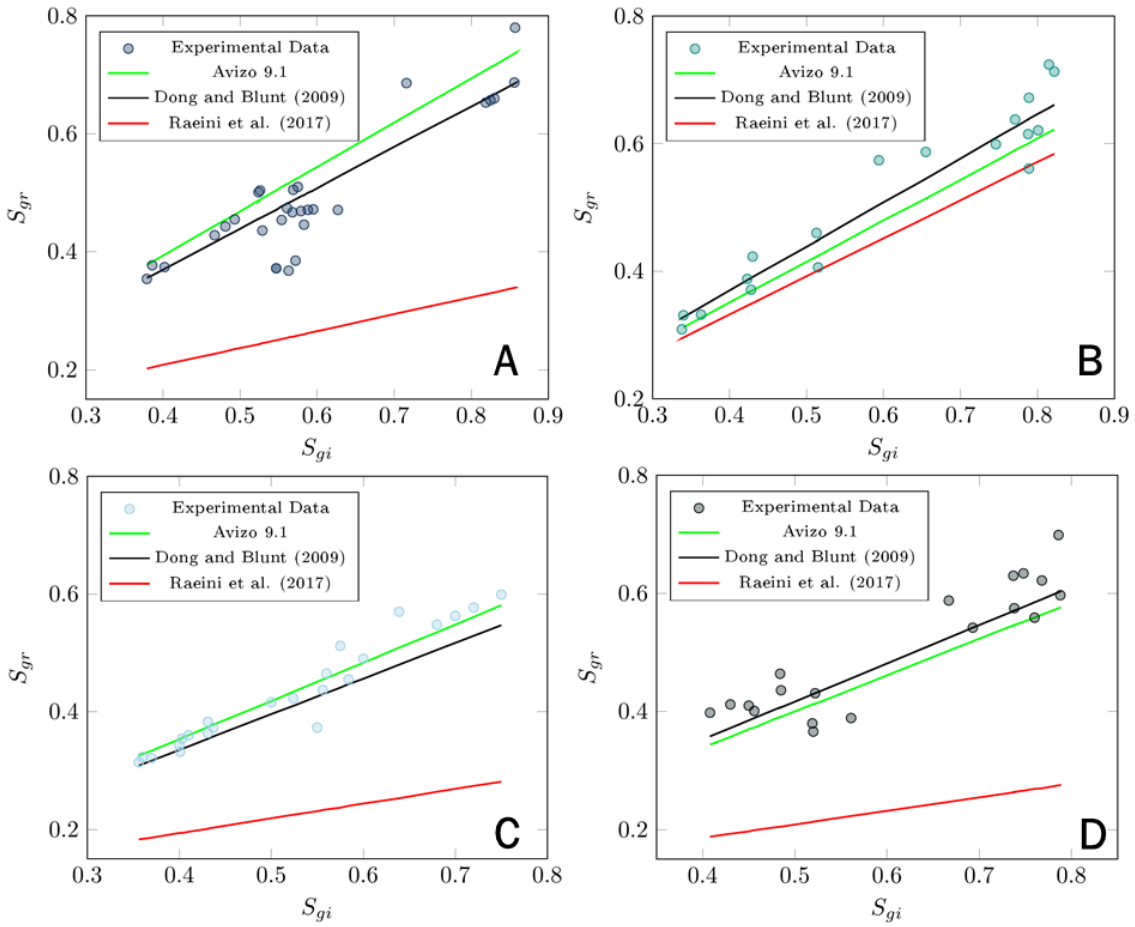

Figure 5.11: Experimental data of the four porous media models compared to the three empirical equations obtained from the three extraction methods.

Figures 5.1-5.6 show that both Avizo 9.1 and Dong and Blunt (2009) gave similar average coordination numbers and average aspect ratio values. On the contrary, the

Raeini et al. (2017) network model average values were highly influenced by the spikes in throat size distributions, which resulted in spikes in the aspect ratio calculations at a low value. However, in the case of the 3D printed model B, the aspect ratio calculation through the Raeini et al. (2017) model did not show a spike at the lower values. It was closer to the average aspect ratio values obtained from Avizo 9.1 and Dong and Blunt (2009) models. Therefore, as shown in **Figure 5.11**, the three extraction methods agreed to estimate the capillary trapping of model B. The agreement in model B values is because of the applicability of the medial-axis method implemented in the Raeini et al. (2017) model on heterogeneous systems. Model B was the most homogenous system, in which the medial-axis method works well in calculating the aspect ratio (estimating the number of pores and throats). When the system's heterogeneity increases, the number of sub-divided throats in the medial-axis method increases since the algorithm-defined corners increase. Therefore, Raeini et al. (2017) used the medial-axis method did not perform well in estimating the capillary trapping of models A, C, and D.

The formulated empirical equation was compared to the widely used Land (1968) and Spiteri et al. (2008) models for capillary trapping estimation. Land (1968) suggested a characteristic shape model, where there is a constant difference between the reciprocals of a system's initial and residual gas saturations. Therefore, Land's model can be summarized in the following equations.

$$S_{gr}^{*} = \frac{S_{gi}^{*}}{1+CS_{gi}^{*}} \tag{5.2}$$

$$C = \frac{1}{S^*_{gr_{max}}} - 1 \tag{5.3}$$

where the C constant value is an iterative process of guessing its value until the squared error between the experimental residual gas saturation S_{gr} and the S^*_{gr} is minimized.

Similarly, Spiteri et al. (2008) used a pore-network model to predict the trapped non-wetting phase saturation as a function of the initial non-wetting saturation. Spiteri's model has two fitting constants, as shown in **Equation 5.4**, and therefore increases the accuracy of the capillary trapping estimation.

$$S_{or} = \propto S_{oi} - \beta_s {S^2}_{oi} \tag{5.4}$$

Land's C constant and Spiteri's $\propto$ and β_s constant values for this model applied to each system are displayed in **Table 5.2**.

Table 5.2: Fitting constants of Land and Spiteri's models based on the presented experimental data.

Model	Land's Model Constant C [-]	Spiteri's Model Constant $\propto$ [-]	Spiteri's Model Constant β_s [-]
A	0.316	0.867	0.059
B	0.270	1.000	0.225
C	0.371	0.917	0.163
D	0.328	0.940	0.179

The empirical equation from this work and Land's model were plotted against the experimental data of each model, as shown in **Figure 5.12**. The pore structure parameter of each model was used from the Avizo 9.1 pore network model since it is the most recent pore network extraction model. The empirical equation formulated in this work provides a reasonable estimate of the capillary data, only based on the

pore structure parameter. It is also important to mention that the two models, Land (1968) and Spiteri et al. (2008), are only fitting models that do not depend on reservoir characteristics such as the pore structure.

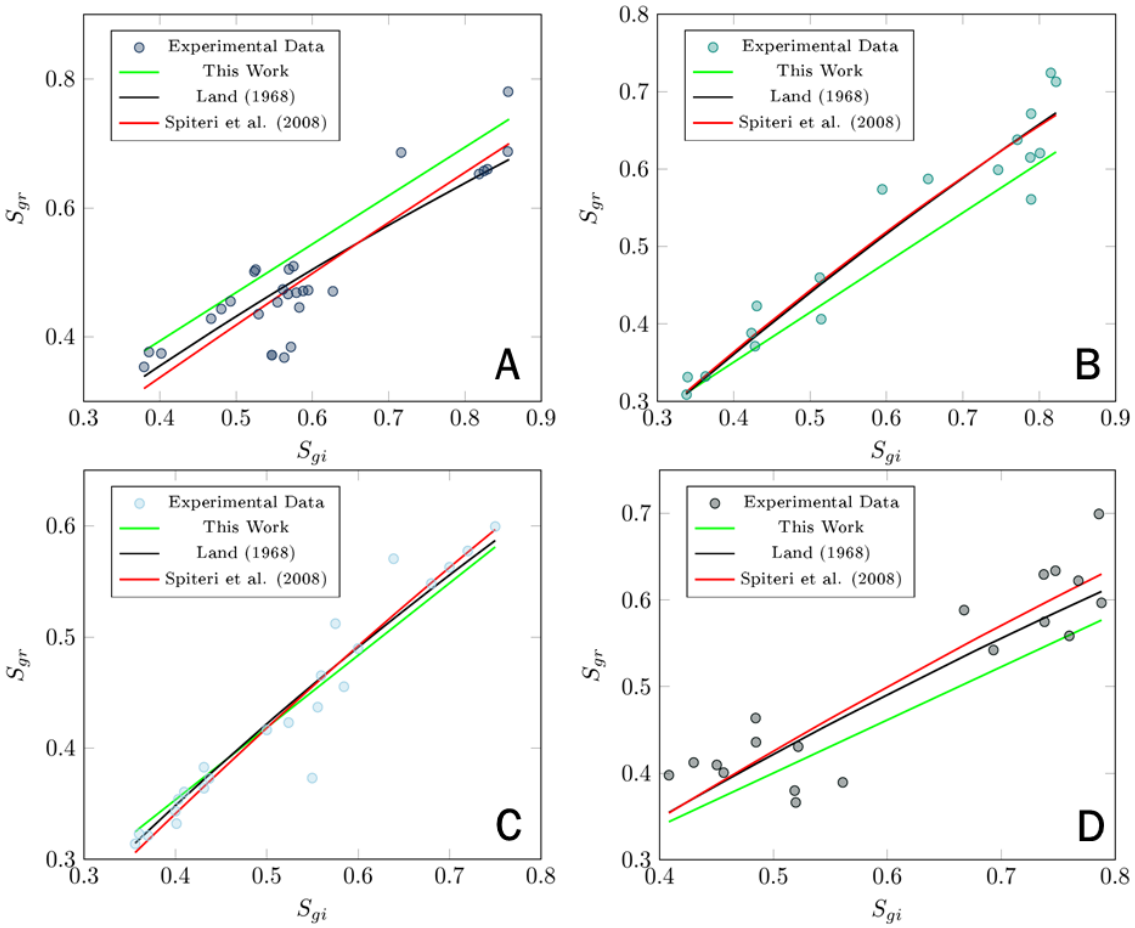

Figure 5.12: Comparing the experimental capillary trapping of models A, B, C, and D, Land's model, Spiteri's model, and the estimated trapping curve using the empirical relationship obtained from this work.

The empirical equation formulated in this work provides a reasonable estimate of the capillary data, only based on the pore structure parameter. The coefficient of determination of the formulated equation, using the extraction outputs from Avizo 9.1, was compared to the coefficients of determination values of Land's and Spiteri's, as shown in **Table 5.3**.

Table 5.3: The coefficient of determination of the two widely used models compared to the one obtained in this study.

Model	Land's Model R^2 [-]	Spiteri's Model R^2 [-]	This Work's R^2 [-]
A	0.675	0.872	0.956
B	0.998	0.967	0.805
C	0.847	0.961	0.821
D	0.762	0.882	0.755
Average	**0.820**	**0.889**	**0.834**

Compared to Land's and Spiteri's fitting models, the equation proposed in this study showed good agreement with the experimental data and had an average coefficient of determination of 0.834, as shown in Table 5.3. However, the advantage of this proposed model is that it purely depends on pore structure inputs, and it is simpler to use for capillary trapping estimation.

6. CONCLUSIONS AND RECOMMENDATIONS FOR FUTURE WORK

The objective of this study was to investigate the effect of pore structure, represented by the average coordination number and average aspect ratio, on capillary trapping in four 3D printed, water-wet porous media. The experiment was done to formulate an empirical equation that estimated the capillary trapping capacity of any water-wet system based on the pore structure only. Both the average aspect ratio and average coordination number of a system directly influence capillary trapping. The outcomes of this work can be summarized in the following points:

1. Generally, the higher the average aspect ratio, the higher the trapping capacity. Throats increase the mobility of the fluids; however, when the pore size is much greater than the throat sizes (high aspect ratio), the non-wetting phase gets trapped inside the pores due to the snap-off effect agrees with the findings mentioned in the literature.
2. The higher the average coordination number, the lower the trapping capacity of the system due to more throats connected to each pore, which allows the non-wetting phase to flow continuously, supported by the literature review.
3. The coordination number alone is a weak indicator of the system's pore structure, and the average aspect ratio of a system has more effect on the capillary trapping capacity.
4. It was found that a higher pore structure parameter β results in higher trapping capacity at higher initial non-wetting phase saturation, which is a unique finding in this study.

5. Based on the results of this study, the pore structure parameter is recommended to be extracted from a model that utilizes the maximal ball algorithm compared to the medial-axis algorithm that overestimated the number of throats in the heterogeneous models.
6. The formulated equation was compared to Land's and Spiteri's models and the experimental data obtained in this work, and it showed good agreement with an average coefficient of determination of 0.83.

This work is the benchmark for deeper analysis into the effect of pore structure on capillary trapping and trapping capacity. This study adds value to the literature regarding pore structure and capillary trapping analysis; nevertheless, it is recommended that this study be extended to oil-water systems to support the findings in the gas-water system. It is also recommended to perform experiments on systems that are not water-wet to generalize the findings. Furthermore, the research should be expanded by adding the effect of varying flow rates, which will change the capillary pressure in the system.

REFERENCES

Agarwal, R. G. (1967). *Unsteady-state performance of water-drive gas reservoirs* /z-wcorg/.

Agbalaka, C. C., Dandekar, A. Y., Patil, S. L., Khataniar, S., & Hemsath, J. (2008). The Effect Of Wettability On Oil Recovery: A Review. SPE Asia Pacific Oil and Gas Conference and Exhibition,

Alley, R., Hewitson, B., Hoskins, B., Joos, F., Jouzel, J., Kattsov, V., Lohmann, U., Manning, M., Matsuno, T., Molina, M., Nicholls, N., Berntsen, T., Overpeck, J., Qin, D., Raga, G., Ramaswamy, V., Ren, J., Rusticucci, M, S., S, Somerville, R., Stocker, T., Stott, P., Bindoff, N., Stouffer, R., Whetton, P., Wood, R., Wratt, D., Chen, Z., Chidthaisong, A., Friedlingstein, P., Gregory, J., Hegerl, G., & Heimann, M. (2007). *Climate Change 2007: The Physical Science Basis, Summary for Policymakers, Intergovernmental Panel on Climate Change: Geneva, CH*.

Alnoush, W., Shaat, A., & Alyafei, N. (2021). *What Is the Optimum Wettability for Oil Recovery Through Waterflooding?* The SPE Conference at Oman Petroleum & Energy Show, Oman.

Alyafei, N. (2015). *Capillary Trapping and Oil Recovery in Altered-Wettability Carbonate Rock* Imperial College London].

Alyafei, N. (2019). *Fundamentals of Reservoir Rock Properties* HBKU Press.

Alyafei, N., Bautista, J., Mari, S., Khan, T., & Seers, T. (2020). *Multi-Dimensional Project Based Learning on Understanding Petrophysical Properties by Utilizing Image Processing and 3D Printing* https://doi.org/10.2118/200549-MS

Anderson, W. G. (1986a). *Nettability Literature Survey-Part 2: Wettability Measurement*.

Anderson, W. G. (1986b). Wettability Literature Survey-Part 1: Rock/Oil/Brine Interactions and the Effects of Core Handling on Wettability. *JPT, Journal of Petroleum Technology, 38*(11), 1125-1144.

Bachu, S., Gunter, W. D., & Perkins, E. H. (1994, 1994/04/01/). Aquifer disposal of CO2: Hydrodynamic and mineral trapping. *Energy Conversion and Management, 35*(4), 269-279. https://doi.org/https://doi.org/10.1016/0196-8904(94)90060-4

Bear, J. (1988). Dynamics of fluids in porous media. http://www.freading.com/ebooks/details/r:download/ZnJlYWQ6OTc4MDQ4NjEzMTgwMTpl

Blunt, M. J., & Scher, H. (1995, 12/01/). Pore-level modeling of wetting. *Physical Review E, 52*(6), 6387-6403. https://doi.org/10.1103/PhysRevE.52.6387

Chiquet, P., Broseta, D., & Thibeau, S. (2007, 2007/05/01). Wettability alteration of caprock minerals by carbon dioxide [https://doi.org/10.1111/j.1468-8123.2007.00168.x]. *Geofluids, 7*(2), 112-122. https://doi.org/https://doi.org/10.1111/j.1468-8123.2007.00168.x

Clifford, S. M., & Hillel, D. (1986). KNUDSEN DIFFUSION: THE EFFECT OF SMALL PORE SIZE AND LOW GAS PRESSURE ON GASEOUS TRANSPORT IN SOIL. *Soil Science, 141*(4). https://journals.lww.com/soilsci/Fulltext/1986/04000/KNUDSEN_DIFFUSION__THE_EFFECT_OF_SMALL_PORE_SIZE.6.aspx

Dake, L. P. (1978). *Fundamentals of reservoir engineering*. Elsevier Scientific Pub. Co. ; Distributors for the U.S. and Canada Elsevier North-Holland.

Dickson, J. L., Gupta, G., Horozov, T. S., Binks, B. P., & Johnston, K. P. (2006, 2006/02/01). Wetting Phenomena at the CO2/Water/Glass Interface. *Langmuir, 22*(5), 2161-2170. https://doi.org/10.1021/la0527238

Dong, H., & Blunt, M. J. (2009, 09/14/). Pore-network extraction from micro-computerized-tomography images. *Physical Review E, 80*(3), 036307. https://doi.org/10.1103/PhysRevE.80.036307

Elbashir, N. O., Al-Zahrani, S. M., Abdul Mutalib, M. I., & Abasaeed, A. E. (2002, 2002/11/01/). A method of predicting effective solvent extraction parameters for recycling of used lubricating oils. *Chemical Engineering and*

Processing: Process Intensification, 41(9), 765-769. https://doi.org/https://doi.org/10.1016/S0255-2701(02)00006-5

Ennis-King, J. P., & Paterson, L. (2005). Role of Convective Mixing in the Long-Term Storage of Carbon Dioxide in Deep Saline Formations. *SPE Journal, 10*(03), 349-356. https://doi.org/10.2118/84344-PA

Espinoza, D. N., & Santamarina, J. C. (2010, 2010/07/01). Water-CO2-mineral systems: Interfacial tension, contact angle, and diffusion—Implications to CO2 geological storage [https://doi.org/10.1029/2009WR008634]. *Water Resources Research, 46*(7). https://doi.org/https://doi.org/10.1029/2009WR008634

Falkowski, P., Scholes, R. J., Boyle, E., Canadell, J., Canfield, D., Elser, J., Gruber, N., Hibbard, K., Högberg, P., Linder, S., Mackenzie, F. T., Moore Iii, B., Pedersen, T., Rosenthal, Y., Seitzinger, S., Smetacek, V., & Steffen, W. (2000). The Global Carbon Cycle: A Test of Our Knowledge of Earth as a System. *Science, 290*(5490), 291. https://doi.org/10.1126/science.290.5490.291

Friedlingstein, P., Houghton, R., Marland, G., Hackler, J., Boden, T., Conway, T., Canadell, J., Raupach, M., Ciais, P., & Le Quere, C. (2010). Update on CO2 emissions. *Nature Geoscience, 3*, 811-912.

Geffen, T. M., Parrish, D. R., Haynes, G. W., & Morse, R. A. (1952). Efficiency of Gas Displacement From Porous Media by Liquid Flooding. *Journal of Petroleum Technology, 4*(02), 29-38. https://doi.org/10.2118/952029-G

Geistlinger, H., Beckmann, A., & Lazik, D. (2005, 2005/11/01). Mass transfer between a multicomponent trapped gas phase and a mobile water phase: Experiment and theory [https://doi.org/10.1029/2004WR003885]. *Water Resources Research, 41*(11). https://doi.org/https://doi.org/10.1029/2004WR003885

Geistlinger, H., Mohammadian, S., Schlueter, S., & Vogel, H.-J. (2014, 2014/05/01). Quantification of capillary trapping of gas clusters using X-ray microtomography [https://doi.org/10.1002/2013WR014657]. *Water Resources Research, 50*(5), 4514-4529. https://doi.org/https://doi.org/10.1002/2013WR014657

Gibbins, J., & Chalmers, H. (2008, 12/01). Carbon capture and storage. *Energy Policy, 36*, 4317-4322. https://doi.org/10.1016/j.enpol.2008.09.058

Gunter, W. D., Perkins, E. H., & McCann, T. J. (1993, 1993/09/01/). Aquifer disposal of CO2-rich gases: Reaction design for added capacity. *Energy Conversion and Management, 34*(9), 941-948. https://doi.org/https://doi.org/10.1016/0196-8904(93)90040-H

Hawkes, C., McLellan, P., & Bachu, S. (2005, 10/01). Geomechanical Factors Affecting Geological Storage of CO2 in Depleted Oil and Gas Reservoirs. *Journal of Canadian Petroleum Technology - J CAN PETROL TECHNOL, 44*. https://doi.org/10.2118/05-10-05

Hernandez, E., Grassia, P., & Shokri, N. (2015). Foam-improved oil recovery: Modelling the effect of an increase in injection pressure. *EUROPEAN PHYSICAL JOURNAL E, 38*(6).

Hoffert, M. I., Caldeira, K., Benford, G., Criswell, D. R., Green, C., Herzog, H., Jain, A. K., Kheshgi, H. S., Lackner, K. S., Lewis, J. S., Lightfoot, H. D., Manheimer, W., Mankins, J. C., Mauel, M. E., Perkins, L. J., Schlesinger, M. E., Volk, T., & Wigley, T. M. L. (2002). Advanced Technology Paths to Global Climate Stability: Energy for a Greenhouse Planet. *Science, 298*(5595), 981. https://doi.org/10.1126/science.1072357

Holtz, M. H. (2005). *Reservoir Characterization Applying Residual Gas Saturation Modeling, Example From the Starfak t1 Reservoir, Middle Miocene Gulf of Mexico* The University of Texas at Austin].

Iglauer, S., Wülling, W., Pentland, C., Mansoori, S., & Blunt, M. (2009, 06/08). Capillary Trapping Capacity of Rocks and Sandpacks. https://doi.org/10.2118/120960-MS

Iglauer, S., Wülling, W., Pentland, C. H., Al-Mansoori, S. K., & Blunt, M. J. (2011). Capillary-Trapping Capacity of Sandstones and Sandpacks. *SPE Journal, 16*(04), 778-783. https://doi.org/10.2118/120960-pa

iglauer, S., Wulling, W., Pentland, C. H., Al Mansoori, S. K., & Blunt, M. J. (2009). *Capillary Trapping Capacity of Rocks and Sandpacks* https://doi.org/10.2118/120960-MS

Jacobs, T. (2020). BP's Energy Outlook Foresees Big Shift for Oil Demand. *Journal of Petroleum Technology, 72*(10), 42-44. https://doi.org/10.2118/1020-0042-jpt

Jerauld, G. R. (1997). Prudhoe Bay Gas/Oil Relative Permeability. *SPE Reservoir Engineering, 12*(01), 66-73. https://doi.org/10.2118/35718-PA

Jerauld, G. R., & Salter, S. J. (1990, 1990/04/01). The effect of pore-structure on hysteresis in relative permeability and capillary pressure: Pore-level modeling. *Transport in Porous Media, 5*(2), 103-151. https://doi.org/10.1007/BF00144600

Joekar-Niasar, V., Hassanizadeh, S. M., & Leijnse, A. (2008, 2008/09/01). Insights into the Relationships Among Capillary Pressure, Saturation, Interfacial Area and Relative Permeability Using Pore-Network Modeling. *Transport in Porous Media, 74*(2), 201-219. https://doi.org/10.1007/s11242-007-9191-7

Joekar Niasar, V. (2010). *The Immiscibles: Capillarity Effects in Porous Media - Pore-Network Modelling* Utrecht University, Geosciences Faculty, Earth sciences department]. Utrecht University, Geosciences Faculty, Earth sciences department.

Kleppe, J., Delaplace, P., Lenormand, R., Hamon, G., & Chaput, E. (1997). *Representation of Capillary Pressure Hysteresis in Reservoir Simulation* https://doi.org/10.2118/38899-MS

Krevor, S., Blunt, M. J., Benson, S. M., Pentland, C. H., Reynolds, C., Al-Menhali, A., & Niu, B. (2015). Capillary trapping for geologic carbon dioxide storage - From pore scale physics to field scale implications. *International Journal of Greenhouse Gas Control, 40*, 221-237. https://doi.org/10.1016/j.ijggc.2015.04.006

Lackner, K. S. (2003). A Guide to CO₂ Sequestration. *Science, 300*(5626), 1677. https://doi.org/10.1126/science.1079033

Land, C. S. (1968). Calculation of Imbibition Relative Permeability for Two- and Three-Phase Flow From Rock Properties. *Society of Petroleum Engineers Journal, 8*(02), 149-156. https://doi.org/10.2118/1942-PA

Lindeberg, E., & Wessel-Berg, D. (1997, 1997/01/01/). Vertical convection in an aquifer column under a gas cap of CO2. *Energy Conversion and Management, 38*, S229-S234. https://doi.org/https://doi.org/10.1016/S0196-8904(96)00274-9

Ma, T. D., & Youngren, G. K. (1994). *Performance of Immiscible Water-Alternating-Gas (IWAG) Injection at Kuparuk River Unit, North Slope, Alaska* https://doi.org/10.2118/28602-MS

Mahani, H., Keya, A. L., Berg, S., Bartels, W. B., Nasralla, R., & Rossen, W. R. (2015). Insights into the mechanism of wettability alteration by low-salinity flooding (LSF) in carbonates. *Energy and Fuels, 29*(3), 1352-1367. https://doi.org/10.1021/ef5023847

Morrow, N. R., Lim, H. T., & Ward, J. S. (1986). Effect of Crude-Oil-Induced Wettability Changes on Oil Recovery. *SPE Formation Evaluation, 1*(01), 89-103. https://doi.org/10.2118/13215-pa

Naar, J., & Henderson, J. H. (1961). An Imbibition Model - Its Application to Flow Behavior and the Prediction of Oil Recovery. *Society of Petroleum Engineers Journal, 1*(02), 61-70. https://doi.org/10.2118/1550-G

Oak, M. J., Baker, L. E., & Thomas, D. C. (1990). Three-Phase Relative Permeability of Berea Sandstone. *Journal of Petroleum Technology, 42*(08), 1054-1061. https://doi.org/10.2118/17370-PA

OrrJr, F. M. (2004, 09/01). Storage of Carbon Dioxide in geologic formations. *JPT, Journal of Petroleum Technology, 56*, 90-97. https://doi.org/10.2118/88842-JPT

Pentland, C. H., El-Maghraby, R., Georgiadis, A., Iglauer, S., & Blunt, M. J. (2011, 12/31). Immiscible Displacements and Capillary Trapping in CO 2 Storage. *Energy Procedia, 4*, 4969-4976. https://doi.org/10.1016/j.egypro.2011.02.467

Pentland, C. H., Itsekiri, E., Al Mansoori, S. K., Iglauer, S., Bijeljic, B., & Blunt, M. J. (2010). Measurement of Nonwetting-Phase Trapping in Sandpacks. *SPE Journal, 15*(02), 274-281. https://doi.org/10.2118/115697-PA

Qi, R., LaFoRCe, T. C., & BLunT, M. J. (2010). Carbon dioxide (CO2) injection design to maximise underground reservoir storage and enhanced oil recovery (EOR). *Woodhead Publishing Limited*.

Rabbani, H. S., Joekar-Niasar, V., Pak, T., & Shokri, N. (2017, 2017/07/04). New insights on the complex dynamics of two-phase flow in porous media under intermediate-wet conditions. *Scientific Reports, 7*(1), 4584. https://doi.org/10.1038/s41598-017-04545-4

Rabbani, H. S., Seers, T. D., & Guerillot, D. (2019). Analytical Pore-Network Approach (APNA): A novel method for rapid prediction of capillary pressure-saturation relationship in porous media. *Advances in Water Resources, 130*(June), 147-156. https://doi.org/10.1016/j.advwatres.2019.05.027

Raeini, A. Q., Bijeljic, B., & Blunt, M. J. (2017, 07/20/). Generalized network modeling: Network extraction as a coarse-scale discretization of the void space of porous media. *Physical Review E, 96*(1), 013312. https://doi.org/10.1103/PhysRevE.96.013312

Ronen, D., Berkowitz, B., & Magaritz, M. (1989). The development and influence of gas bubbles in phreatic aquifers under natural flow conditions. *Transport in Porous Media, 4*(3), 295-306.

Schembre-McCabe, J. M., Kamath, J., & Gurton, R. M. (2007). Mechanistic Studies of CO2 Sequestration. International Petroleum Technology Conference,

Spiteri, E., Juanes, R., Blunt, M., & Orr, F. (2008, 09/01). A New Model of Trapping and Relative Permeability Hysteresis for All Wettability Characteristics. *SPE Journal - SPE J, 13*, 277-288. https://doi.org/10.2118/96448-PA

Stocker, T. F., D. Qin, G-K. Plattner, M. M. B. Tignor, S. K. Allen, J. Boschung, A. Nauels, Y., & Xia, V. B., and P. M. Midgley. (2013). Climate Change 2013: The Physical Science Basis.

Tanino, Y., & Blunt, M. J. (2012). Capillary trapping in sandstones and carbonates: Dependence on pore structure. *Water Resources Research, 48*(8). https://doi.org/https://doi.org/10.1029/2011WR011712

Tanino, Y., & Blunt, M. J. (2013). Laboratory investigation of capillary trapping under mixed-wet conditions. *Water Resources Research, 49*(7), 4311-4319. https://doi.org/https://doi.org/10.1002/wrcr.20344

Tohidi, B, J. Yang, M. Salehabadi, R. Anderson, & A. Chapoy. (2010). CO2 hydrates could
provide secondary safety factor in subsurface sequestration of CO2. *Environ. Sci. Technol.*

Treiber, L. E., & Owens, W. W. (1972). A Laboratory Evaluation of the Wettability of Fifty Oil-Producing Reservoirs. *Society of Petroleum Engineers Journal, 12*(06), 531-540. https://doi.org/10.2118/3526-PA

Wigley, T. M. L., Richels, R., & Edmonds, J. A. (1996, 1996/01/01). Economic and environmental choices in the stabilization of atmospheric CO2 concentrations. *Nature, 379*(6562), 240-243. https://doi.org/10.1038/379240a0